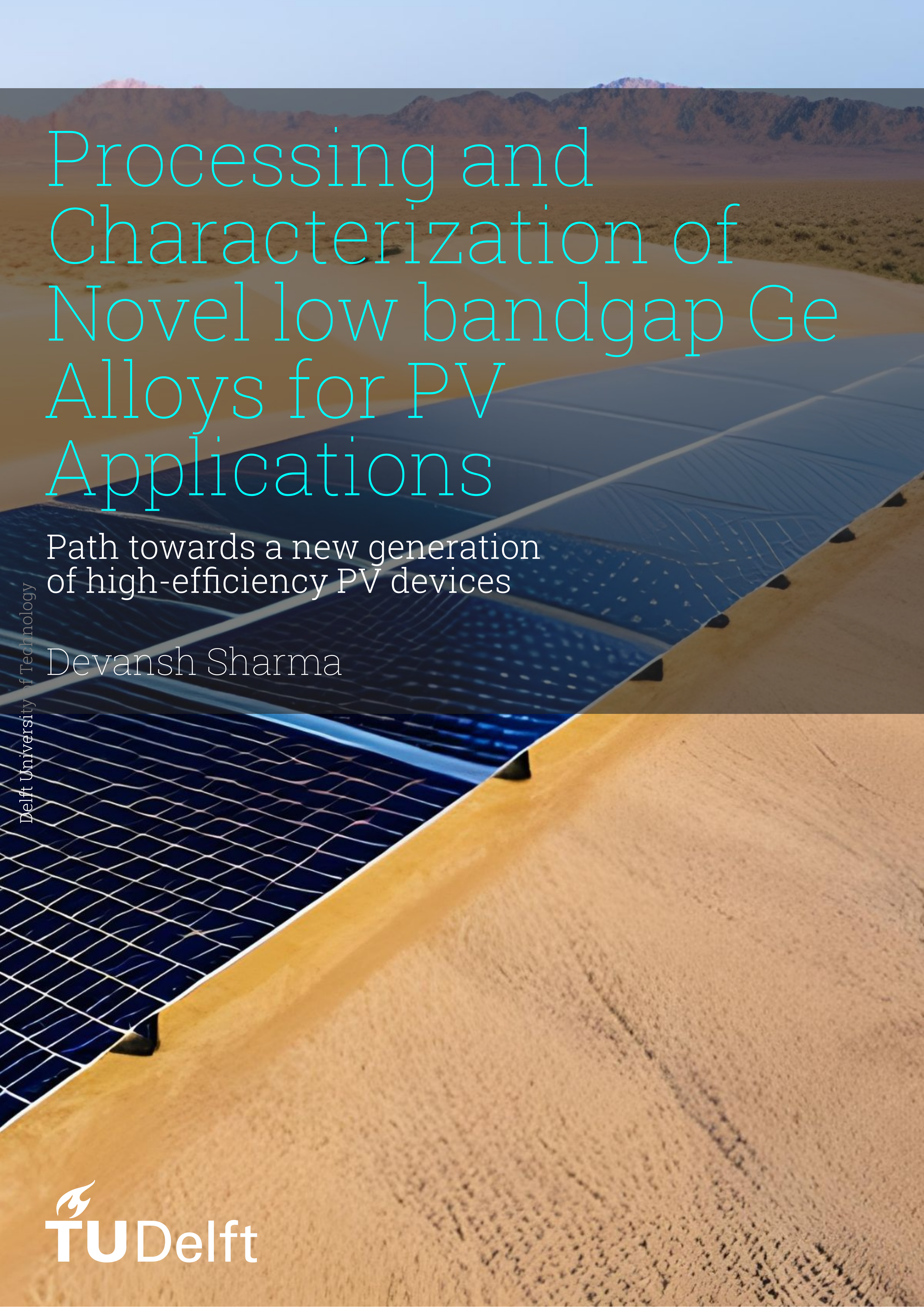

Processing and Characterization of Novel low bandgap Ge Alloys for PV Applications

Path towards a new generation of high-efficiency PV devices

Devansh Sharma

Delft University of Technology

TUDelft

Processing and Characterization of Novel low bandgap Ge Alloys for PV Applications

Path towards a new generation of high-efficiency PV devices

by

Devansh Sharma

to obtain the degree of Master of Science
in Sustainable Energy Technology
at the Delft University of Technology

Student number:	5476305	
Project duration:	November 30, 2022 – July 3, 2023	
Thesis committee:	Prof. dr. ir. A.H.M. Smets	Supervisor
	Dr. Ir. T.J. Savenije	
	Dr. Ir. R. Santbergen	
	Dr. Ir. P. Perez-Rodriguez	Daily Supervisor

TU Delft

Preface

Dear Reader,

This report was written as a submission towards my Master of Science in Sustainable Energy Technology (SET) program at the Delft University of Technology. The research was conducted as part of a larger research on thin-film PV technologies in the Photovoltaic Material and Devices (PVMD) group at the Department of Electrical Engineering, Mathematics and Computer Science (EEMCS). I worked under the daily supervision of Dr Paula P. Rodriguez and was guided by Prof. Arno Smets.

The report presents the steps in depositing and making intrinsic germanium layers for PV applications. While writing this report, I assume that the reader has basic knowledge of solar cell physics or has enough curiosity to learn about it. It is organized in such a way that the reader can follow the problem statement to the results in a step-wise manner. The table of contents has been added to navigate the reader to the desired part of the report.

Readers who wish to revise their basic knowledge can read chapter-2. Readers interested in the design and methodology of the experiments can find it in chapter-3. Chapter 4 presents the findings in detail with reasoning for future researchers to ponder. I hope the findings of this research will advance the process of realizing the next generation of PV cells. With this motivation, I invite you to appreciate the work done by the academic community working towards the energy transition.

Devansh Sharma
Delft, June 2023

Acknowledgements

I want to express my sincere gratitude to everyone who supported me throughout these two years and made it possible for me to complete my master's degree in Sustainable Energy Technology with a sane state of mind.

I moved from India to the Netherlands with a heavy heart of leaving the comfort zone of my home, motivated by a thirst for knowledge that could only be fulfilled by going through this journey of ups and downs. I have seen myself grow academically, personally, and professionally in completely unexpected ways. It would have been impossible without the people I met throughout these two years who made it such an enriching experience.

I want to start by expressing my heartfelt gratitude towards Prof. Arno Smets, who inspired me to pursue challenging problem statements right from the first quarter, starting with the course on Renewable Energy followed by PV Technologies. His enthusiasm for teaching and knack for the subject is quite contagious. Thank you for supporting me in deciding to work on this topic and being there in numerous brainstorming sessions and evening chats that kept my enthusiasm high. I would also like to thank Dr Paula Rodriguez, who has been a constant support and an incredible guide throughout the eight months of this research. It was my immense pleasure to work with you. I also want to thank Dr Gianluca Limodio, Govind Padmakumar, and all the staff at the PVMD Group for sharing their experience and helping me whenever I got stuck. I would also like to thank all my fellow students who distracted me with some interesting and sometimes nonsensical fun lunch sessions.

I would also like to extend sincere gratitude to my family and friends. Thank you, Gaurav, Shantiswaroop and Shloka, for being the constant team throughout this academic journey. I also want to thank Janki, Kishan, Ritik and Utkarsh for being there in the most trying and good times. I could never ask for better friends with whom I have made some of my best memories. Finally, yet most importantly, I want to thank my family for being the constant emotional support and cheerleaders who pushed me to be my best. It would not have been possible without any of you.

Abstract

This thesis aimed to process and characterize hydrogenated germanium (Ge:H) films to use them as a low-bandgap intrinsic absorber layer. The bandgap of Germanium can go up to 0.67 eV. A p-i-n solar cell consisting of intrinsic germanium film produced using Plasma Enhanced Chemical Vapour Deposition (PECVD) can be inexpensively paired with crystalline silicon and other semiconductor materials to produce a multijunction solar cell with high efficiencies. Such a cell would utilize the lower part of the solar spectrum currently untapped in commercially available mass-produced solar modules. Previous research had deposited Ge:H films using a direct PECVD reactor as compared to a showerhead configuration in the reactor used in this research.

The study consisted of two experiments that explored the properties of the germanium film deposited. First, the deposition parameters of PECVD were varied to study its effect on important film properties. Since the material will be used for low-bandgap applications, the optical bandgap (E_{04}) and activation energy were the most important parameters to monitor film quality. Secondly, two sets of experiments were performed to understand the degradation in properties of the intrinsic films when exposed to environmental factors. Two types of degradation are studied: light-induced degradation and oxidation in air.

Power, pressure, germane to hydrogen flow ratios, deposition time, substrate temperature and ignition time of the plasma to introduce gases was varied across 30 samples to define an ideal processing regime. A small processing window was identified where intrinsic amorphous germanium (a-Ge:H) films were produced. The lowest E_{04} achieved for intrinsic films was 0.8 eV with an activation energy of 0.39 eV which lies at the centre of the bandgap.

The degradation experiments showed no sign of oxygen signature from EdX measurements performed after two months and FTIR measurements performed after two weeks. Light-induced degradation (LID) was performed by exposing the samples for over 80 hours; photoconductivity did not degrade below the initial value for the duration of the exposure.

Thus, the results look promising in proving these films as a suitable material for an intrinsic absorber layer. It also shows that the showerhead PECVD configuration can lead to better control of reaction mechanics giving films with desired material properties. The layer can be used as an intrinsic layer in a p-i-n structure device, paving the way for a new generation of high-efficiency multijunction solar PV devices.

Contents

List of Figures

List of Tables

1

Introduction

Solar power is the most abundant energy source to fulfil humanity's rising energy needs. The incident solar energy on the planet is known to be 10000 times the power consumed by mankind currently. Photovoltaic (PV) devices have been the holy grail of converting solar power into a secondary energy carrier, i.e. electricity. First-generation devices, consisting of crystalline silicon (c-Si) solar modules, are mass-produced and are used on a vast scale. One drawback of using these modules is the thickness which adds to material cost and allows the production of only rigid modules. Moreover, these devices have a high content of glass and metal due to the supporting frame, which affects the profitability of recycling these modules at their end of life. [9]

Thin-film devices are the second generation of PV devices which are lightweight and flexible. In this technology, the absorbing material in the solar cell is typically 100 times thinner than the c-Si counterparts [45]. This allows much lesser use of material to encapsulate the solar cell and develop its mounting structure. Over the years, the cost of producing these modules has been reduced, leading to cheaper modules. However, the efficiency of these devices, which measures how effectively sunlight is converted to electricity, is relatively low compared to their first-generation counterparts. Yet, with the possibility of adding multiple layers, the efficiency can be increased to reach higher values [34].

A multijunction solar cell is a device that consists of multiple layers of semiconductors stacked on top of each other. The layers are designed to absorb different portions of the solar spectrum, increasing the overall efficiency of the solar cell. Many approaches have been explored to develop low-cost high-efficiency devices, some of which that can pair with c-Si, to utilize the high bandgap region of the solar spectrum and prevent thermalization losses. Examples of these are perovskites [8], III-IVs [43] and the a-Si:H/nc Si:H micromorph tandem solar cells [31].

In all these devices, the lower part of solar spectra with energy photons lower than 1.1 eV is not utilized. This is lost as below bandgap losses. In the spectral range of 0.7eV-1.1eV, the AM1.5G solar spectrum provides approximately $9.92 \cdot 10^{20} s^{-1} \cdot m^{-2}$ photons. This corresponds to a current density of $15.9 mA \cdot cm^{-2}$ [57]. Developing a low bandgap absorber material that can tap this part of the spectrum would pave the way for higher efficiencies. The current density available in this region of the solar spectrum would allow the development of the bottom layer in a multifunction device which will not be currently limiting.

Germanium is an excellent candidate for this purpose as a group IV element with a low bandgap. It is scarce but not extremely rare [12]. It has an indirect bandgap of 0.67 eV and a direct bandgap of 0.8 eV, which places it ideally to utilize the Infrared region of the solar spectrum. Germanium is recognized for its high charge carrier mobilities, which has allowed for its use in high-speed electronics [60]. Therefore, very thin layers of Ge can be incorporated into solar cells allowing low material use. Thin films can be used in devices with a p-i-n structure where the material has an amorphous or micro-crystalline structure. Such a structure requires the incorporation of hydrogen (forming the :H in Ge:H) to produce alloys with low defect densities. The hydrogen passivates the dangling bonds in the non-crystalline structure. Hydrogenated germanium (Ge:H) can be inexpensively processed using a widely known industrial process, Plasma Enhanced Chemical Vapour Deposition (PECVD).

1.1. Research objectives and outline

To develop germanium-aided high-efficiency thin-film devices, this research focuses on creating a hydrogenated germanium absorber layer that can be used as an intrinsic layer in a p-i-n structure device. Previous research in the group has developed films that were processed using a direct PECVD reactor [57]. It was observed that post-deposition oxidation played a major role in degrading the material properties. This research uses a showerhead PECVD reactor that can lead to better control of reaction mechanics and films with desired material properties.

This study explores the development of hydrogenated amorphous germanium by thoroughly characterizing and analyzing various processing conditions. To that end, the following three research questions are addressed:

1. What are the deposition conditions for obtaining intrinsic germanium films?
2. What is the influence of light and exposure to air on the films?
3. Has the showerhead configuration helped in improving the quality of films?

The report is structured in the following manner. Chapter 2 gives the background information followed by Chapter 3 which discusses the methodology of the processing and characterization. Results and discussion are covered in Chapter 4. Finally, Chapter 5 concludes the findings and provides recommendations for future research.

2

Background

This chapter outlines the theoretical foundations required to understand the research conducted. One should start by looking at the solar spectrum to understand the importance of developing a low-bandgap material. An explanation of solar cell thin-film technologies follows this. Section 3 explains the manufacturing process used in this research i.e. Plasma Enhanced Chemical Vapour Deposition (PECVD). The final section investigates the properties of Germanium and its potential as a low bandgap material.

2.1. Solar energy and the photovoltaic effect

The solar spectrum refers to the range of electromagnetic radiation emitted by the Sun, including both visible and non-visible wavelengths. The Sun emits a continuous spectrum of light, with wavelengths ranging from about 100 nm to over 1 millimeter. This spectrum can be divided into several regions based on wavelength, including ultraviolet (UV), visible, and infrared (IR).

The UV portion of the solar spectrum, which includes wavelengths below 400 nm, is largely absorbed by the Earth's atmosphere. This is fortunate, as UV radiation can harm human health and damage living organisms and materials. The IR portion of the solar spectrum, which includes wavelengths above 700 nm, is largely absorbed by the Earth's atmosphere as well. However, some longer-wavelength IR radiation is able to penetrate the atmosphere and contribute to the Earth's greenhouse effect, warming the planet's surface. Thus, the sunlight that reaches the atmosphere is different from that reaching the earth's surface. These are called air mass 0 (AM0) spectrum and AM1.5 spectrum, respectively and are illustrated in Figure 2.1.

Sunlight is composed of packets of energy called photons. The energy of each photon is governed by its wavelength and can be described by the following equation:

$$E = \frac{hc}{\lambda} \tag{2.1}$$

Here, h is the plank's constant, c is the speed of light and λ is the wavelength of the photon. There are multiple photons at each wavelength, and the power density or irradiance in Figure 2.1 is affected by the number and energy of photons of that wavelength. The number of photons per unit area per second, also known as spectral photon flux can be determined by dividing the power density per wavelength of light by the energy per photon of light as per the equation:

$$\Phi(\lambda) = P(\lambda)\frac{\lambda}{hc} \tag{2.2}$$

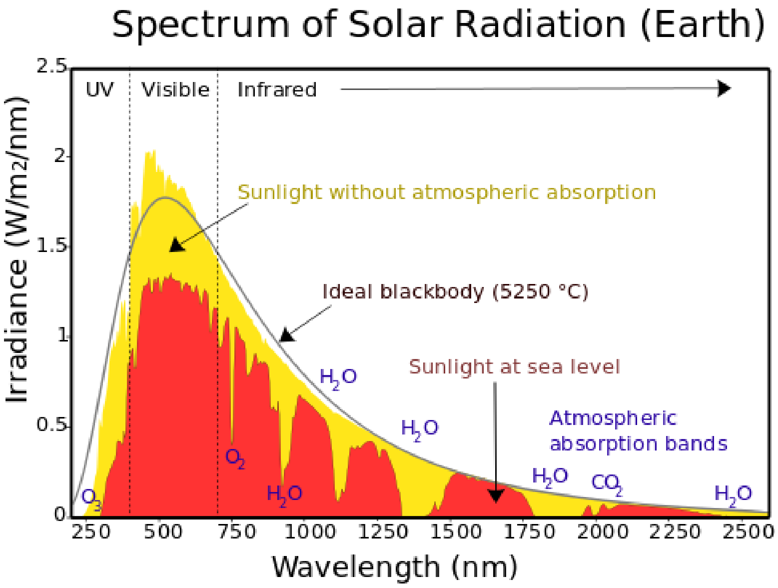

Figure 2.1: Solar spectrum: yellow region is AM0, red region is AM1.5 and black line represents the profile of an ideal blackbody at sun's surface temperature [7]

2.1.1. Photovoltaic effect

Solar cells absorb only a part of the AM1.5 spectrum based on the bandgap of the absorber material. Bandgap can be understood by knowing the concept of energy bands. An atom's electrons can only occupy a limited number of discrete energy levels, with ”forbidden states” representing intermediate energy levels that cannot be achieved. At lower energy levels, electrons are bound to the nucleus, while higher energy levels allow electrons to break free. When atoms bond covalently to form larger structures, new energy states arise that fill the gaps between the original levels, creating energy bands. Two types of energy bands exist: the valence band for valence electrons involved in bonding and the conduction band for unbound energy states where electrons can move freely in a crystal lattice.

Conductors have overlapping bands, so electrons can easily transition from bound to unbound states with little energy difference, making them highly conductive. In the case of insulators and semiconductors, there are forbidden energy states between the two types of bands described earlier, forming the bandgap. An electron can make a transition from the conduction band to the valence band, provided it receives more energy than the bandgap. Bandgap E_G is calculated as the difference between the conduction band edge E_C and valence band edge E_V.

$$E_G = E_C - E_V \tag{2.3}$$

Bandgap is usually expressed in electron volt (eV). Materials with large bandgaps require a large amount of energy to excite the electrons, and thus, insulators have these properties. Bandgaps of different types of materials can be seen in Figure 2.2.

Solar cells operate by absorbing photons emitted by the sun that have higher energy than the material's bandgap, causing a valence electron to move to the conduction band. At room temperature, some covalent bonds break due to thermal energy, promoting electrons to the conduction band, a process known as generation. Electrons can move freely, leaving behind a vacancy or hole, which can be filled by another valence electron, resulting in the movement of the hole. Generation creates an electron-hole pair, and vacancies can also be filled by electrons from the conduction band, known as recombination. A material is known to be in

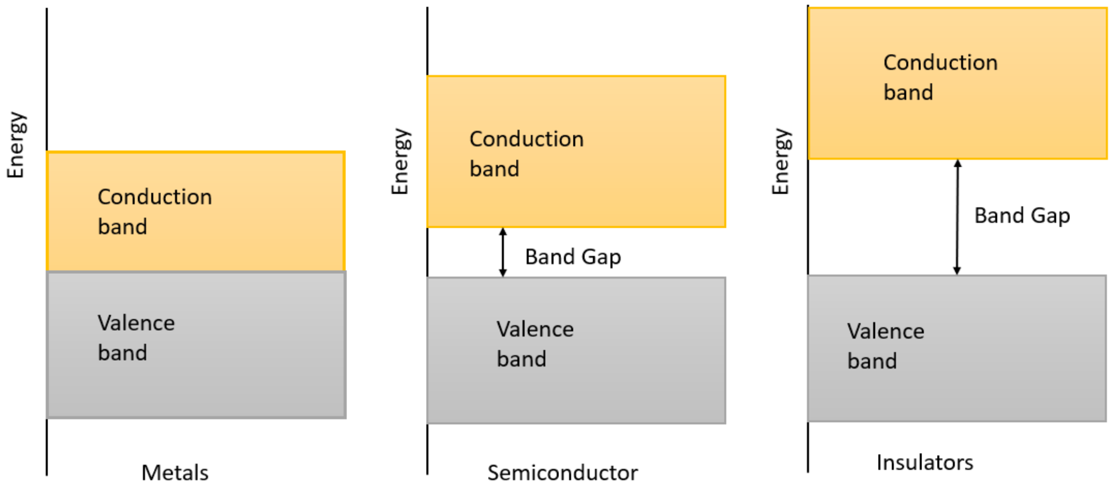

Figure 2.2: Energy bands of insulators, semiconductors and metals

thermal equilibrium when there is no external energy input and recombination and generation rates even out. The Fermi-Dirac distribution describes the probability of a specific energy state being occupied by holes or electrons in thermal equilibrium. The average energy of electrons in the conduction and valence band put together is known as the fermi energy (E_F).

The value of the Fermi energy level at room temperature depends on the specific material being considered. In intrinsic semiconductors (pure materials without any doping), the Fermi level is generally located approximately halfway between the conduction band and valence band energies at room temperature. However, in doped semiconductors (materials with impurities introduced intentionally to alter their electrical properties), the Fermi level can be shifted up or down depending on the type and concentration of dopants.

2.1.2. p-i-n junction

The p-i-n junction is a type of structure used in thin-film solar cells to create a built-in electric field that separates photogenerated electron-hole pairs and drives them to the contacts to produce electricity. It has three layers described here with an example of an a-Si thin-film solar cell.

- P-layer: The p-layer, or p-type layer, is made from a semiconductor material that has an excess of positively charged holes. This is achieved by doping the material with impurities such as boron, which creates ”holes” in the valence band of the semiconductor, where electrons are normally absent.
- i-layer: The i-layer, or intrinsic layer, is made from a semiconductor material that is undoped or lightly doped, which means it has an equal number of electrons and holes. When sunlight strikes the i-layer, it generates electron-hole pairs.
- n-layer: The n-layer, or n-type layer, is made from a semiconductor material that has an excess of negatively charged electrons. This is achieved by doping the material with impurities such as phosphorus, which creates ”free” electrons in the conduction band of the semiconductor.

The p-i-n junction is created by stacking the three layers in the order of p-i-n. The p-layer and n-layer are typically made thinner than the i-layer. Although some electron-hole pairs will be created in the p- and n- layers, their main function is to create an electric field to separate the charges created in the i-layer. Typical materials used are SiO_x and SiC, which have a high bandgap energy and therefore absorb as little light as possible. They also tend to have more recombination sites because of the doping, so they are as thin as possible. A schematic and the band diagram of the p-i-n junction can be seen in Figure 2.3.

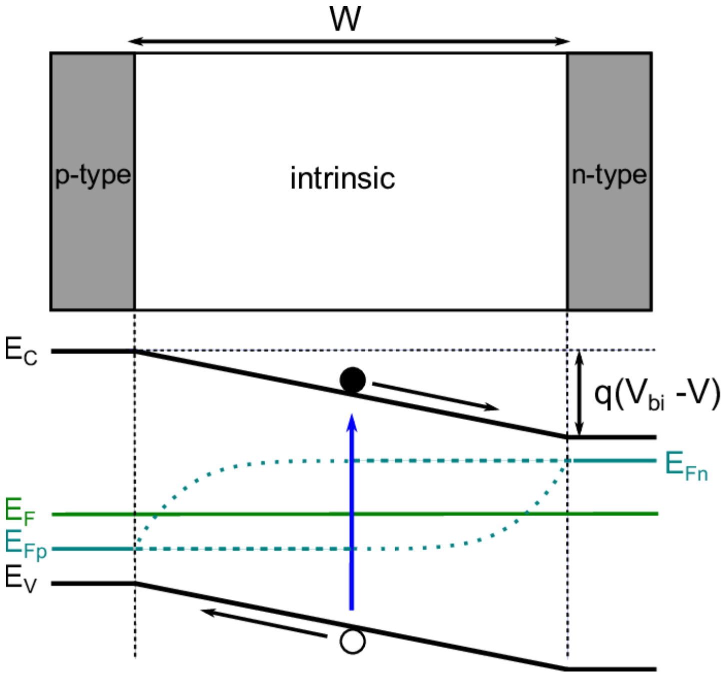

Figure 2.3: Band diagram of a p-i-n junction [28]

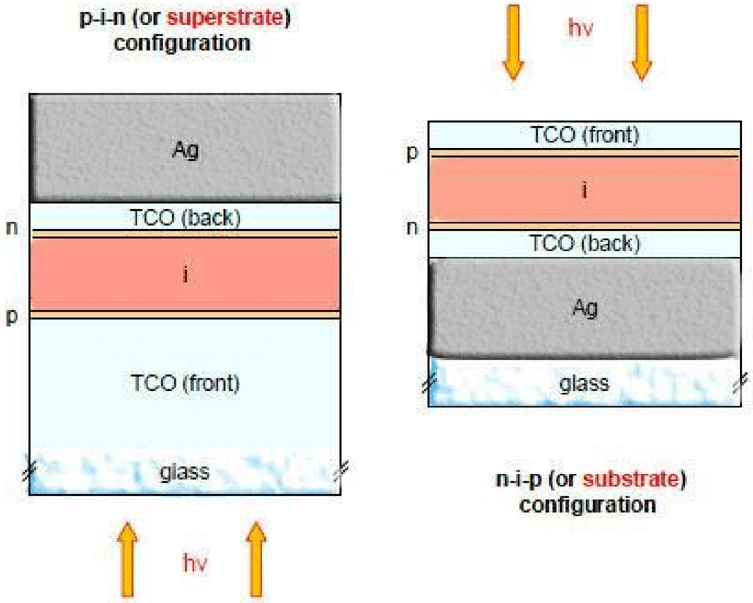

Figure 2.4: Thin-film solar cells in superstrate and substrate configuration [35]

When the layers are deposited in the order of p-i-n, the solar cell is said to be deposited in the superstrate configuration. This means that the first layer deposited is also the layer through which light enters the solar cell. Since glass forms the first layer, a conductive transparent layer is deposited before the p-layer to collect the holes. This is called the transparent conductive oxide, and is typically formed of metal oxide with large bandgap that allows it suppress any parasitic absorption of sunlight. Thin-film solar cells can also be deposited in the n-i-p order, also known as the substrate configuration. Both configurations are illustrated in Figure 2.4.

2.2. Photovoltaic Technologies

Many technologies capture solar energy using the photovoltaic effect. They differ in the types of material used and performance under sunlight. This section explains the generations of solar cells and expands on the properties of multi-junction devices.

2.2.1. Generations of solar cells

Over the years, there have been several generations of solar cells developed, each with its own set of advantages and disadvantages. Here is a brief explanation of each generation of solar cells:

1. First Generation Solar Cells (1950s-2000s): First-generation solar cells are made from crystalline silicon, which is the most common material used for solar cells. These cells have high efficiencies, with conversion rates of up to 26.81% [4]. However, they are also expensive to produce and require a lot of energy to manufacture.
2. Second Generation Solar Cells (2000s-2010s): Second-generation solar cells are made from thin-film materials such as cadmium telluride (CdTe), copper indium gallium selenide (CIGS), or amorphous silicon (a-Si). These materials are cheaper to produce than silicon, and they can be applied to flexible substrates. However, their efficiency is slightly lower than that of first-generation cells, with the best efficiency of 23.54% achieved by CIGS solar cells [54]
3. Third Generation Solar Cells (2010s-Present): Third-generation solar cells are being developed to improve the efficiency and cost-effectiveness of solar energy. These cells use advanced materials such as perovskites, which are cheaper to produce than silicon and have the potential for higher efficiency. However, perovskite solar cells are still in the early stages of development, and their long-term stability and durability are not yet fully understood [30].
4. Fourth Generation Solar Cells (Future): Fourth-generation solar cells are still in the research and development phase. These cells aim to address the limitations of previous generations by using advanced materials such as graphene, metal oxides and technologies such as nanotechnology and biotechnology [36]. Some potential options for fourth-generation cells include organic photovoltaics and biohybrid solar cells.

Overall, each generation of solar cells has brought improvements in efficiency, cost, and flexibility, and the development of new materials and technologies will continue to drive innovation in solar energy.

2.2.2. Structure and properties of multi-junction devices

The new generations of solar cells have a long way to go when it comes to acquiring a higher market share and gaining popularity as a reliable product. Take the example of thin-film devices that form the second generation of solar cell technology. The promise of the cheap, lightweight and flexible nature of these devices promoted much research into realising these cells. However, crystalline silicon still leads the installed capacity with a market share of roughly 95% [18]. Two major factors have prevented the large-scale implementation of these devices. One is the availability of materials used in these solar cells. Cadmium telluride (CdTe) cells have the element Tellurium which has very low availability. Copper Indium Gallium Selenide (CIGS) solar cells also face the same issue as they use Indium which is a rare element [47]. The second issue lies with the performance of these cells. The highest reported efficiency for CdTe cells is 21.57% [14], for CIGS is 23.54% [54] whereas, for a-Si, this number falls to 13.6% [41].

Multi-junction solar cell devices, also known as tandem solar cells, are advanced photovoltaic devices that have revolutionized the field of solar energy harvesting. These devices are capable of achieving significantly higher conversion efficiencies compared to traditional single-junction solar cells. The key principle behind multi-junction solar cells is the use of multiple semiconductor layers stacked on top of each other, each with different bandgap energy. Utilizing multiple layers with different bandgaps can capture a broader range of the solar spectrum, leading to improved efficiency.

Several technologies have been developed to create multi-junction solar cell devices, each employing various semiconductor materials and fabrication techniques. Here are some notable examples:

III-V Compound Semiconductor Technology: This technology utilizes compound semiconductors from the III-V group of the periodic table, such as gallium indium phosphide (GaInP), gallium indium arsenide (GaInAs), and gallium arsenide (GaAs). These materials offer excellent optoelectronic properties and can absorb different portions of the solar spectrum. III-V compound semiconductor-based tandem cells can achieve record-breaking efficiencies by carefully designing the layer thickness and bandgap energies. For instance, in 2022, a research team at the Fraunhofer ISE achieved a new efficiency record of 47.6% for a four-junction solar cell at a concentration of 665 sun illumination[1]. This breakthrough utilized a combination of III-V compound semiconductors, gallium indium phosphide (GaInP) and aluminum gallium arsenide (AlGaAs) bonded by Soitec onto a lower tandem solar cell made of gallium indium arsenide phosphide (GaInAsP) and gallium indium arsenide (GaInAs), to achieve unprecedented efficiency [20].

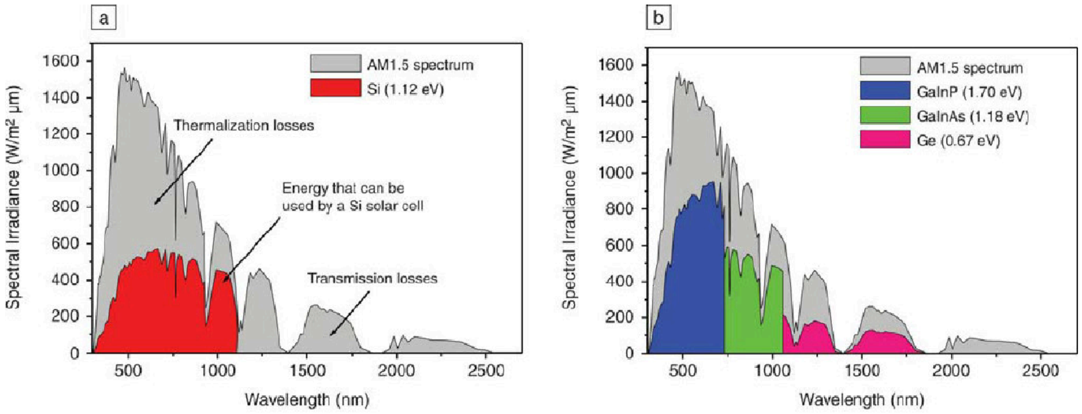

Figure 2.5: Solar spectrum utilization achieved by c-Si (left) and III-V multifunction device with Germanium substrate (right)

---

[1] *Concentrated Photovoltaics (CPV):* CPV systems use lenses or mirrors to concentrate sunlight onto small, high-efficiency multi-junction solar cells. By concentrating the light, the size and cost of the solar cell can be reduced while maintaining high conversion efficiencies. CPV systems often employ multi-junction solar cell technologies to maximize power output

III-V technology has also been combined with Germanium to produce high-efficiency multijunction devices [15]. This cell uses GaInP/GaInAs/Ge subcells to achieve a device with an efficiency of 41.1% under concentrated illumination of 454 suns. This efficiency is realised through current matching and the employment of buffer layers to overcome lattice mismatching of different materials. The spectral utilization of this device can be seen in Figure 2.5.

Perovskite-Silicon Tandem Cells: Perovskite solar cells have gained significant attention due to their low-cost fabrication and high power conversion efficiencies. Researchers have successfully combined perovskite solar cells with traditional silicon solar cells to create tandem structures. The perovskite layer absorbs high-energy photons, while the silicon layer captures lower-energy photons. This combination allows for broader solar spectrum absorption, leading to impressive efficiency improvements. Furthermore, in recent years, perovskite-silicon tandem cells have garnered attention for their impressive progress. In 2023, a perovskite-silicon tandem cell produced by KAUST Photovoltaics Laboratory (KPV-Lab) achieved an efficiency of 33.2%, breaking the previous record for a two-terminal tandem device [21]. This achievement highlights the potential of combining emerging perovskite technologies with established silicon-based solar cells.

Micromorph Solar Cells: Micromorph solar cells are a type of tandem solar cell that combines amorphous silicon (a-Si) and microcrystalline silicon (µc-Si) layers to improve the efficiency of solar energy conversion. The term ”micromorph” refers to the structure of the cell, with the thin layers of amorphous and microcrystalline silicon deposited on top of each other. The crystal structure of these two materials is seen in Figure 2.6. The micromorph design takes advantage of the complementary properties of a-Si and µc-Si. Amorphous silicon absorbs higher-energy photons more efficiently, while microcrystalline silicon is better suited for capturing lower-energy photons. By stacking these two layers, a broader portion of the solar spectrum can be absorbed, increasing the overall efficiency of the solar cell. Micromorph solar cells have demonstrated efficiencies of up to 14% [31].

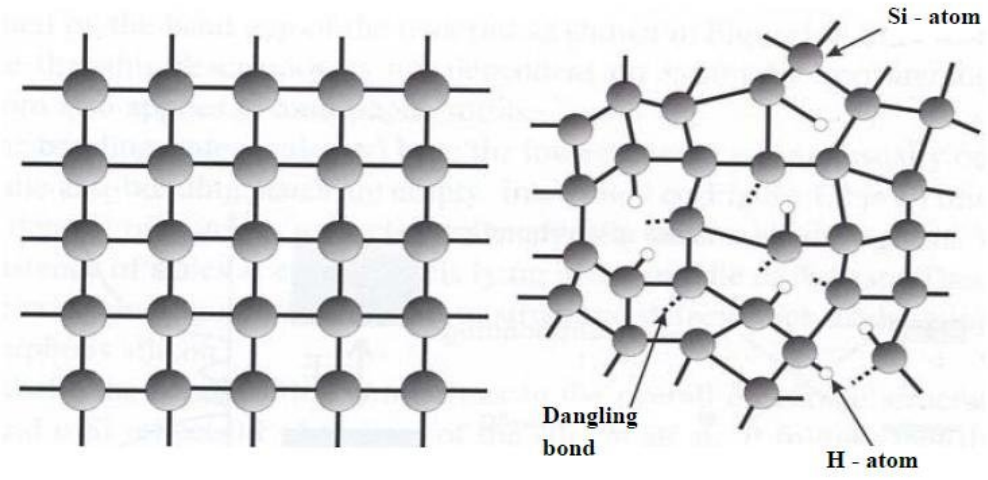

Figure 2.6: 2D representation of Crystalline silicon (left) and amorphous silicon (right) [13]

Currently, the micromorph solar cell, along with the perovskite and c-Si tandem solar cell, does not use the infrared region of the solar spectrum. Germanium has shown potential as a low-bandgap material in III-V solar cells. If another bottom layer of germanium with a lower bandgap can be added to these devices, the efficiency is expected to go higher. These devices can, thus, become more competitive in multijunction PV technology.

2.3. Properties of Germanium and potential as a low-bandgap material

Germanium is a semiconductor material with properties intermediate between a metal and an insulator. In the crystalline form, it has a structure similar to diamond and silicon, with four valence electrons forming covalent bonds with neighbouring atoms. However, it can also have an amorphous structure, just like silicon.

One of the key properties of germanium as a semiconductor material is its small bandgap of around 0.67 eV in the crystalline form. This bandgap is indirect. This means that the minimum energy point of the conduction band and the maximum energy point of the valence band occur at different momentum values in the reciprocal lattice. In other words, the electron transitions between the valence band and the conduction band involve a change in momentum, making the process less likely to occur compared to direct bandgap materials. It requires relatively low energy to excite an electron from the valence band to the conduction band. This makes germanium less efficient than silicon for some applications. Still, it also means that it can be used for applications with low-energy photons, such as in infrared detectors [44]. Germanium has a direct bandgap state of 0.8 eV. Both the bandgaps can be seen in the band structure (Figure 2.7), showing the energy levels with the wavevector. The wave vector, often represented by the symbol ”k,” is a mathematical quantity that characterizes the momentum of a particle, such as an electron, in the crystal lattice of the material.

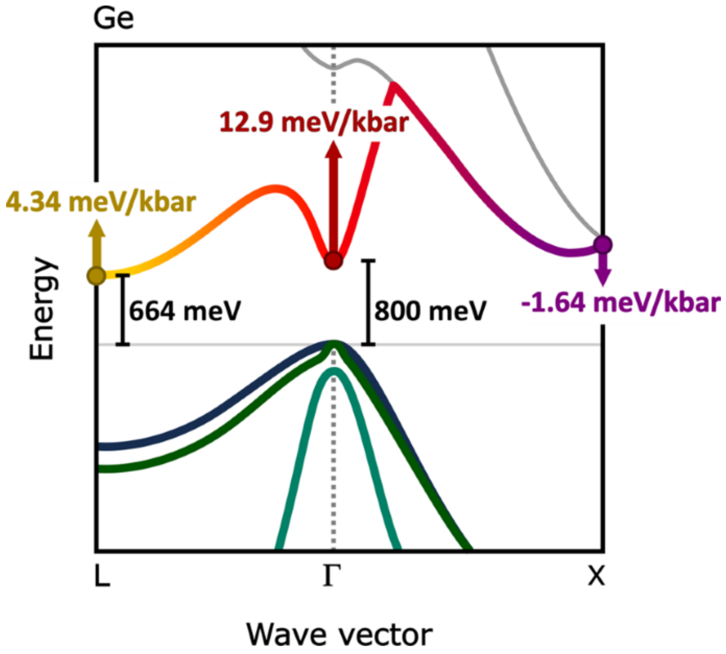

Figure 2.7: Schematic of germanium band structure showing different types of energy transitions [11]

Another important property of germanium is its electron mobility, which is the ability of electrons to move through the crystal lattice. Germanium has a high electron mobility compared to many other semiconductors, meaning electrons can move quickly through the material. Germanium has, thus, become a good choice for applications requiring high-speed electronics, such as in some transistors [60].

These properties make germanium an ideal candidate as a bottom cell for PV applications. Germanium has been used in high-efficiency multijunction solar cells where Ge is used as the substrate [53]. However, the use of germanium as a low bandgap material for solar cells is limited by its high cost and difficulty growing high-quality germanium crystals. Therefore, germanium is typically used only in high-efficiency, niche applications, such as in space-based solar panels, where its superior performance justifies the higher cost [10]. The best configuration cell using GaInP/InGaAs/Ge structure has obtained an efficiency of 31.7% under one sun AM0 illumination [24].

To use germanium in large-scale PV applications, one must use techniques that are cheap and use germanium in very low quantity. Thin-film devices manufactured using PECVD offer the advantage of industry-proven techniques and low material use. Such a solar cell consisting of hydrogenated germanium alloys would be an inexpensive addition as a bottom layer for applications in silicon devices such as the micromorph cell described in subsection 2.2.2. German Aerospace Center (DLR) has demonstrated a-Ge:H cells with an efficiency of 4% with this method [3]. This research used an ultrathin n-i-p configuration in their devices.

2.4. PECVD

Germanium thin films can be produced using various deposition techniques depending on the specific requirements and application. These include Chemical Vapor Deposition [32], Molecular Beam Epitaxy [19], Physical Vapor Deposition methods, such as magnetron sputtering [38] and evaporation [50] and electrochemical deposition [16]. Films deposited using Physical Vapor Deposition techniques were done on silicon substrates, where contamination at the silicon-germanium interface affects the crystal growth [16]. Molecule Beam Epitaxy is performed under extreme vacuum conditions $(10^{-8}\,torr)$, slowing down the deposition process compared to other techniques. The films produced are of high quality, but the manufacturing cost can be high. Moreover, electrochemical deposition produced contaminated films with signatures of N, C and O with a low reaction current efficiency, leading to high energy consumption [16].

Plasma Enhanced Chemical Vapor Deposition (PECVD) is a thin-film deposition process that uses plasma to enhance the chemical reaction between gases and substrate material, creating a thin film on the surface of the substrate. PECVD is commonly used in semiconductors to deposit thin films of various materials, including silicon dioxide, silicon nitride, and amorphous silicon. In PECVD, a vacuum chamber is filled with a mixture of gases, typically consisting of a precursor gas and a reactive gas. An electric field is applied to the gas mixture, creating a plasma that dissociates the precursor gas molecules into reactive species, which then react with the reactive gas to form a solid thin film on the surface of the substrate.

PECVD has several advantages over other thin-film deposition techniques, including low substrate temperatures, which allow deposition onto temperature-sensitive materials, and high deposition rates, which can increase production efficiency. Additionally, the use of plasma can enhance the chemical reactivity of the gas mixture, allowing for the deposition of high-quality thin films with excellent uniformity and conformity [58].

PECVD is widely used in the production of microelectronic devices, such as integrated circuits, flat panel displays, and solar cells, where the ability to deposit high-quality thin films is critical to the performance and reliability of the device. Due to its wide use and advantages over other manufacturing techniques, PECVD is a suitable process to deposit Ge thin films for large-scale solar PV applications.

3

Methodology

The first step to producing a good thin-film solar cell is to develop an intrinsic absorber layer with the required properties. The first section describes previous attempts at producing hydrogenated germanium alloys and experiments conducted in this research to improve the material further. One can characterize such a film using various techniques described in the second section.

3.1. Depositing the germanium intrinsic layer

This section describes the steps followed to deposit the intrinsic germanium layer. Important parameters of the Plasma Enhanced Chemical Vapor Deposition process that can affect the materials are described. This is followed by previous research findings describing the potential conditions that can produce a good film. Finally, the design of experiments followed in this research is described.

3.1.1. Ge:H Deposition

Germanium thin films are deposited on 1.1 mm thick corning gorilla glass for most measurements, except for (100) silicon wafers used for FTIR measurement (refer 3.2), using the AMIGO machine (see Figure 3.1) that performs PECVD deposition. There are seven main parameters that can affect the material properties:

1. Germane (GeH_4) flow: This is the germanium precursor gas that dissociates when added to the plasma. Germanium atoms then combine with each other to form the layer on the glass substrate. In some cases, the gas may not dissociate completely resulting in radicals such GeH_3 which also form a part of the layer.
2. Hydrogen (H_2) flow: Apart from hydrogen originating from GeH_4, hydrogen flow helps in passivating the dangling germanium bonds at the edge of crystals forming the Ge:H alloy.
3. Forward Power: This is the RF power that is applied to the plasma through the electrodes
4. Pressure: This is the pressure in the chamber where the deposition takes place.
5. Deposition Time: It is the time that the plasma stays on. The deposition is performed during this time and can affect the thickness of the material.
6. Temperature: This is the temperature of the substrate.
7. Electrode Distance: This is the gap between the two electrodes in the deposition chamber. The capacitance is affected by this parameter resulting in variation in the intensity of the electric field.

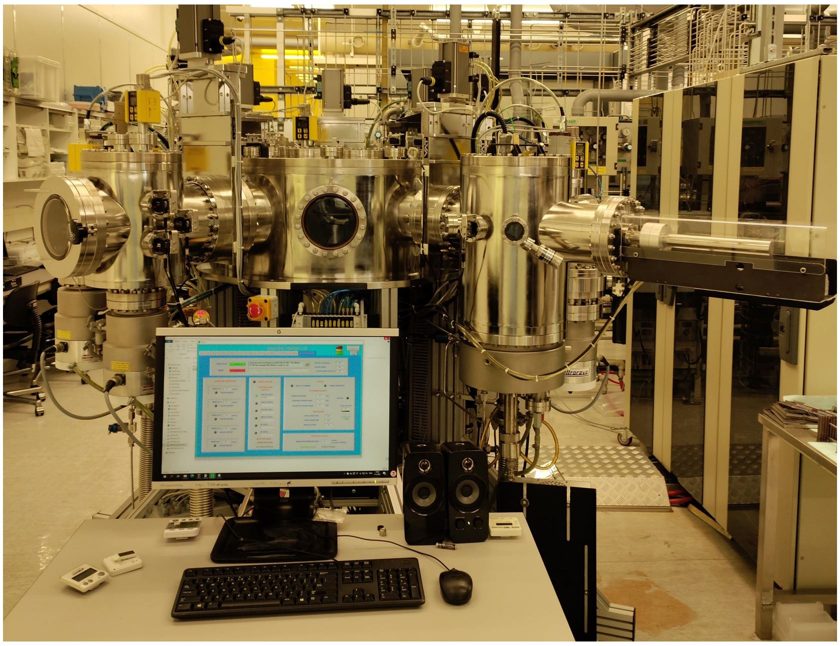

Figure 3.1: The AMIGO machine used to perform the PECVD depostions

3.1.2. Previous research and obtaining initial conditions for deposition

Hydrogenated germanium has been deposited by using several manufacturing techniques in the past, such as RF [6] and DC magnetron sputtering [42], thermal evaporation [49] and glow discharge chemical vapour deposition [26]. The first research [6] characterized the density of the films albeit the densest films produced were really thick ($\sim$40 μm) for thin-film PV applications as the defect density would limit the output current. The second research showed that incorporating oxygen into the samples reduces their activation energy, rendering them more n-type. [42]. The last two research [49] [26] show a dependence of substrate temperature on the crystal quality of the deposited films. Amorphous films are produced at low substrate temperatures ($\sim$200°C), whereas high temperatures ($\sim$ 400-500°C) produce highly crystalline films.

Some work has also been performed on RF PECVD processing of thin film germanium [37] [57]. This research also corroborates the dependence of temperature on material properties such as density and crystallinity. Moreover, it was found that as the electrode spacing increases, the photoelectronic properties of the material tend to decline.

3.1.3. Design of experiments

The initial temperature and electrode distance value were obtained from previous research [57]. It was observed that samples processed at 275 °C and the smallest electrode gap possible for the reactor showed a refractive index ($n_{@600nm}$) above 4.65 irrespective of changes in other parameters. $n_{@600nm}$ has been used as an indication of material density in a variety of materials such as thin evaporated glass films [33] and hydrogenated silicon [39]. The parameters were then varied to optimize the layer based on the refractive index, activation energy and bandgap of the material obtained. All the seven parameters affecting the film properties, except electrode distance, are varied in this research.

Previous research in the group [57] used a PECVD reactor with background gas injection. This research uses showerhead PECVD configuration instead of background gas injection. The showerhead typically comprises a gas distribution plate facing the substrate and an electrode. The gas distribution plate has a series of evenly distributed gas holes or nozzles through

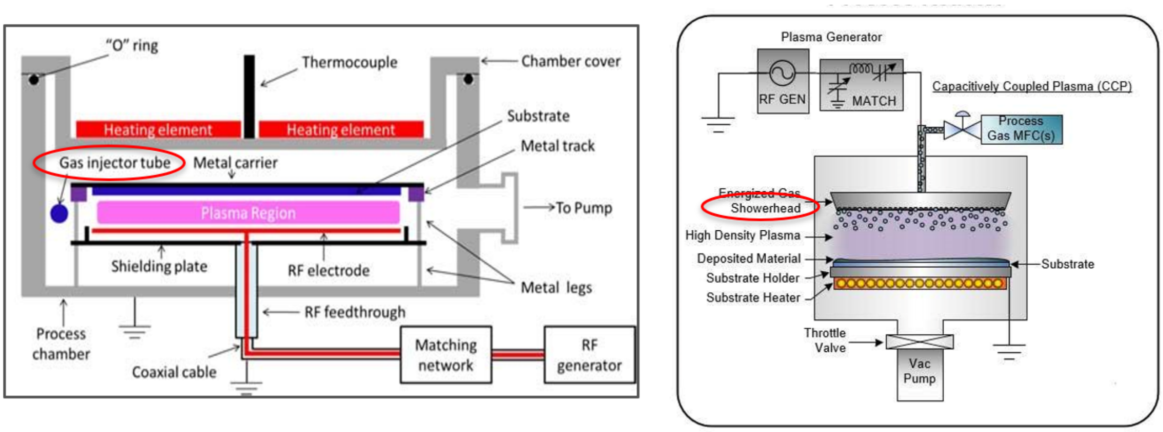

Figure 3.2: Schematic of background gas injection (left) [25] and showerhead PECVD configuration (right) [17]

which process gases are introduced into the reaction chamber. These holes are strategically designed to ensure a uniform gas flow and distribution over the substrate surface. A uniform plasma generation should ensure consistent and controlled film deposition onto the substrate. This is illustrated in Figure 3.2

The values of each parameter used are described in chapter 4 along with the observations of the experiment. The series of experiments conducted varied the following parameters:

1. Pressure
2. Power
3. Germane to hydrogen flow ratios
4. Time of deposition
5. Substrate Temperature
6. Time of ignition of the plasma with respect to the introduction of the gases

It is important to expand on the last parameter. Typically, the plasma is ignited when the deposition chamber is completely occupied with the reactant gases, i.e., an earlier injection (valves are opened 15 mins before ignition). In some depositions, the plasma was ignited right (10 s) after the gases entering the chamber, hence the earlier ignition. This experiment explored the effect where background gases are not present in the chamber. Thus, no gases are ”sucked into” the plasma regime when plasma is ignited.

3.2. Intrinsic Layer Characterization

Intrinsic layer characterization refers to the analysis and evaluation of the properties and performance of the intrinsic layer within a solar cell. The intrinsic layer, also known as the absorber layer or active layer, is a key component of a solar cell that absorbs sunlight and generates electron-hole pairs, which are then used to generate electricity. The important properties of the intrinsic layer are measured using seven different techniques as described in this section.

3.2.1. Spectroscopic Ellipsometry

Spectroscopic ellipsometry (SE) is a sophisticated scientific technique used to investigate the optical properties of materials. It involves shining polarized light onto a sample and analyzing how the light’s polarization changes upon interacting with the material. Valuable information about the material’s composition, structure, and behaviour can be obtained by measuring the changes in the amplitude and phase of the reflected or transmitted light. ESM-300 spectroscopy ellipsometer manufactured by J.A. Woollam Co., Inc. was used to make the measurements (Figure 3.3).

Figure 3.3: Spectroscopy Ellipsometer

The following properties are determined using this technique:

Refractive Index

The refractive index describes how much the material bends light. This can affect the path length of light and therefore, a higher refractive index material would slow down the propagation of light. The refractive index is commonly denoted by the symbol *n*. This value is essential in characterizing the optical parameters of the film and can often be used as a rough indication of the density of the film [29].

The refractive index changes depending on the wavelength of light. [**Born2000**] This means certain materials may allow red light to travel faster than blue light. As a result, different materials exhibit varying levels of reflection across other parts of the electromagnetic spectrum. Thus, choosing one wavelength to consider for the measurements is essential. A wavelength of 600 nm is used in this research.

Thickness and Bandgap

Moreover, spectroscopic ellipsometry can be used to analyze complex, multi-layered structures. By carefully modelling the interaction of light with each layer, one can extract information about the thickness and optical bandgap of individual layers within the structure. The bandgap, thus obtained called the optical bandgap E_{04}, is the energy at which the absorption coefficient reaches a value of 10^4 cm^{-1}. The modelling is done using Cody-Lorentz fitting.

By measuring these values at different points of the thin film, one can also determine the uniformity of the properties with the position of deposition. This is important when assessing the homogeneity and reproducibility of the deposition.

3.2.2. Reflectance and Transmittance measurements

Reflectance, transmittance, and absorptance refer to the optical properties of the films that determine how it interacts with light. These properties are crucial for the efficiency of a solar cell made using these films in converting sunlight into electricity.

1. Reflectance: Reflectance (%R), also known as reflection or reflectivity, measures the amount of incident light reflected off the surface of a solar cell. It represents the percentage of light that is not absorbed and transmitted by the cell but instead bounces back or is scattered away. A lower reflectance value is desirable, as it indicates that more light passes through the absorber layer and is utilized for energy conversion.

2. Transmittance: Transmittance (%T) refers to the ability of the film to allow light to pass through it without being absorbed or reflected. It is the percentage of incident light that is transmitted through the layer.

3. Absorbance: Absorptance (%A) measures the portion of incident light absorbed by the layer. A higher absorptance value indicates that the layer effectively absorbs a larger portion of the incident light and converts it into usable energy. A simple equation can be used to obtain this value.

$$\%A = 100 - \%R - \%T \tag{3.1}$$

All these values vary with the wavelength of light. These measurements are performed using the Lambda 1050+ UV/VIS/NIR spectrometer (Figure 3.4). UV-Vis-NIR spectroscopy is an analytical technique that measures the percentage of discrete wavelengths of UV or visible light absorbed by or transmitted through a sample compared to a reference or blank sample.

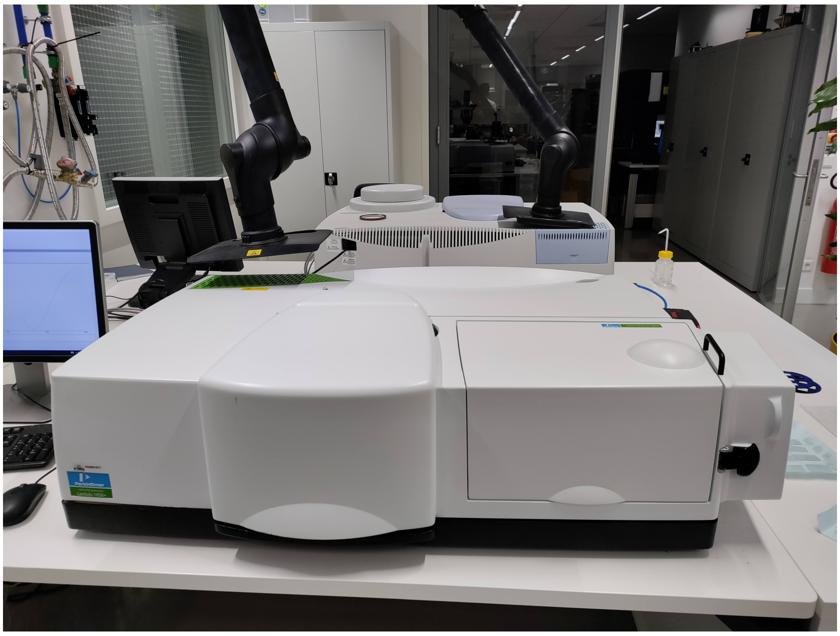

Figure 3.4: Lambda 1050+ UV/VIS/NIR spectrometer

3.2.3. Activation Energy and Conductivity

The activation energy (E_{act}) refers to the minimum energy required to liberate an electron from its bound state and allow it to move freely within the material. To be an effective absorber material, the activation energy should be within a specific range. If the activation energy is too high, only high-energy photons can generate electron-hole pairs, resulting in limited efficiency and poor utilization of lower-energy photons. On the other hand, if the activation energy is too low, thermal energy alone may be sufficient to liberate electrons, causing excessive leakage currents and decreased efficiency.

In the case of intrinsic materials, this value should be as close to half of the bandgap of the material (E_{gap}). To this end, a parameter named intrinsicity is defined to characterise the material. If this value is close to 0.5, the material is considered to be highly intrinsic. Bandgap used for this calculation is the one obtained from SE measurements.

$$Intrinsicity = \frac{E_{act}}{E_{gap}} \tag{3.2}$$

The activation energy can be influenced by various factors, such as the material's band structure, impurities, and defects. It is typically determined experimentally by analyzing the temperature dependence of the material's electrical conductivity or by studying the behaviour of photocurrent under different illumination conditions.

To measure the dark conductivity, 300nm-thick parallel electrodes made of aluminium were evaporated onto the germanium thin films. Samples were annealed at 130^{o}C for 45 mins to fix the contacts. Dark conductivity (σ_d) was then obtained by current measured at different temperatures descending from 130^{o}C to 60^{o}C in intervals of 5^{o}C. Voltage was fixed at 10 V throughout the measurement, and samples were placed in a dark environment. Activation energy at 25 °C and pre-exponential factor σ_0 can then be calculated by the Arrhenius equation:

$$\sigma_d = \sigma_0 exp(\frac{-E_{act}}{k_b T}) \tag{3.3}$$

Photoconductivity (σ_{ph}) was also measured for a few samples to understand the performance of the material under illumination. It is obtained by measuring the current through the electrodes using four-point probes by varying the voltage from -1 V to 1 V under AM1.5 illumination of 100 mW/cm^2 and a controlled stage temperature of 25^{o}C. Resistance (R) of the sample, thus, obtained can be used to calculate the photoconductivity using the equation:

$$\sigma_{ph} = \frac{l}{R.A} \tag{3.4}$$

where l is the distance between the electrodes and A is the area of the region of the cell illuminated, i.e., the area between the electrodes.

3.2.4. Raman Spectroscopy

Raman Spectroscopy is a technique used to analyze the molecular composition and structure of materials by studying the scattering of light. It involves illuminating a sample with a laser and detecting and analyzing the scattered light. The scattered light carries information about the vibrational modes of the molecules in the sample, providing insights into their chemical composition and molecular bonding. By examining the shifts in energy and intensity of the scattered light, scientists can identify the types of molecules present and gain valuable information about their structural characteristics, such as chemical bonds and crystal symmetry.

Renishaw InVia confocal Raman microscope was used in this research to obtain the measurements with an Argon green laser operating at a wavelength of 514.5 nm. The spectra are fitted with Gaussian distributions at Raman shifts of 177 cm^{-1}, 230 cm^{-1} and 278 cm^{-1} corresponding to amorphous germanium stretching modes [27] and another Gaussian at 300 cm^{-1} for crystalline germanium peak at 300 cm^{-1} [2]. The Gaussians are fit using Fityk freeware [59]. Crystallinity (X$_C$) can then be calculated as

$$X_C = \frac{I_{c-Ge}}{I_{c-Ge} + \gamma.I_{a-Ge}} \tag{3.5}$$

Figure 3.5: RAMAN Microscope

Where I$_{c-Ge}$ is the integrated area of Gaussian of crystalline germanium and I$_{a-Ge}$ is the area of Gaussian of a-Ge TO mode, the largest of a-Ge stretching modes. γ corresponds to a correction factor for the difference in phonon excitation of c-Ge concerning a-Ge. A value of 0.85 is used. This method is reused from previous research [57].

3.2.5. X-Ray Diffraction (XRD)

X-ray diffraction (XRD) is a powerful analytical technique used to study crystal structure and properties of materials. It involves shining X-rays onto a sample and analyzing the resulting diffraction pattern to obtain information about the arrangement of atoms within the material. Information about the crystal lattice parameters, such as unit cell dimensions, symmetry, and atomic positions within the crystal, can be obtained by analysing the diffraction pattern, which consists of characteristic peaks. A typical XRD pattern of nano-crystalline and amorphous germanium is shown in Figure 3.6 for reference. Diffraction peaks at 27.15°, 45.30° and 53.65° can be observed if the material is polycrystalline and no peaks are seen if the material is amorphous [55].

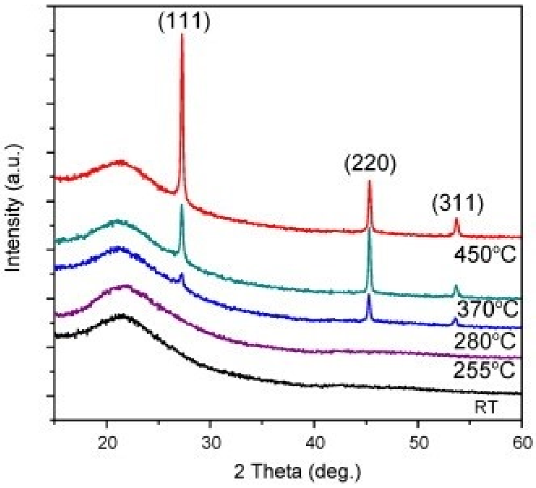

Figure 3.6: X-Ray Diffraction Pattern of nanocrystalline (top 3 curves) and amorphous germanium (bottom two curves) [55]. The bump observed around 22° comes from the glass substrate.

3.2.6. Fourier Transform Infrared Spectroscopy (FTIR)

Fourier Transform Infrared Spectroscopy (FTIR) is a powerful technique used for material characterization. It involves analyzing the interaction of the material with infrared light to understand its composition and structural properties. FTIR can provide detailed information about the chemical bonds and functional groups by subjecting the material to a broad range of infrared wavelengths and applying a mathematical technique called the Fourier transform. This information is crucial for evaluating the performance and efficiency of solar cells, as it helps identify impurities, defects, and degradation mechanisms that may affect their overall functionality.

To prepare the samples for this measurement, germanium is deposited on (100) oriented crystalline silicon wafers. These wafers are then compared with a sample crystalline silicon wafer from the same batch to remove the background spectrum. This measurement is used to identify the presence of oxygen caused by the oxidation of germanium, indicating the chemical stability of the material. One can also identify Ge:H stretching modes located at 560 cm^{-1}, 1875 cm^{-1} and 1980 cm^{-1}. A typical FTIR spectrum seen for an oxidized germanium film can be seen in Figure 3.7.

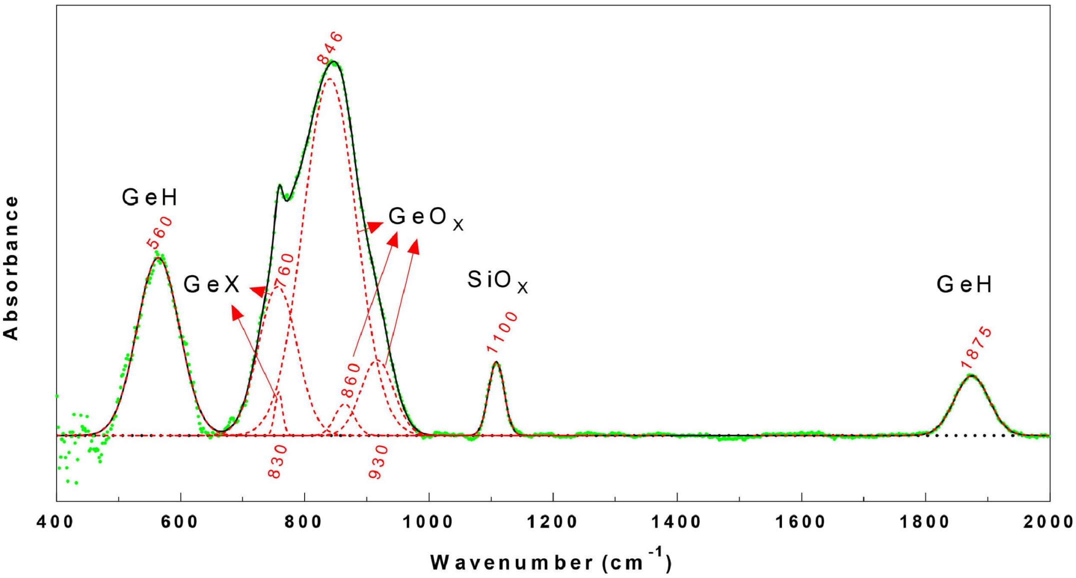

Figure 3.7: Fitted FTIR spectrum of a typical Ge:H film after oxidation [57]

3.2.7. Energy Dispersive X-ray Spectroscopy (EDX)

Energy Dispersive X-ray Spectroscopy (EDX) is a technique used to analyze the elemental composition of a material by detecting characteristic X-rays emitted when the material is exposed to high-energy X-ray radiation. In this research, it is used to detect oxidation in the thin-film material. Oxygen has characteristic X-ray emission lines that are distinct from the other elements in the film. The degree of oxidation can be assessed by measuring the intensity and distribution of these oxygen X-rays. The typical sensitivity of EDX measurements is 1% atomic weight.

4

Results

This section presents the results obtained from experiments described in subsection 3.1.1 per characterization techniques described in section 3.2. They are explained in five sections. The first section covers the homogeneity of the films, second section describes the crystal structure of the material, third section covers the experimental results of varying different parameters and the fourth section explores the stability of the material. Lastly, the results are discussed to answer the three research questions described in the introduction.

4.1. Homogeneity of films

In the initial set of experiments, germanium films were deposited on 10cm x 10cm corning gorilla glass. This size of sample would cover the full area of the substrate holder in the PECVD chamber. It was done to determine whether the films have uniform material properties throughout the deposition area. After the films were deposited, SE measurements were taken for 9 points spread uniformly across the sample as illustrated in Figure 4.1.

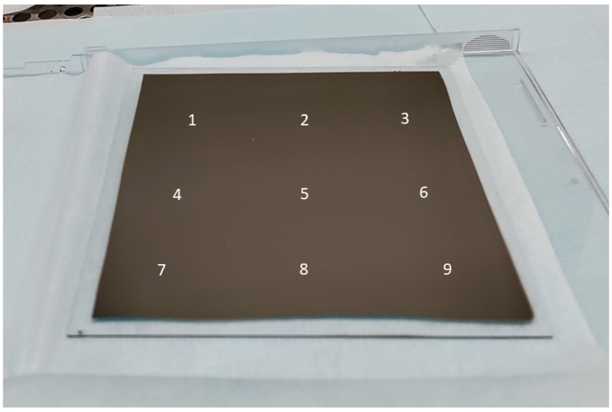

Figure 4.1: Points of measurement on the germanium film

Thickness was used as the parameter to understand the homogeneity of films. It was calculated for each point with respect to the centre of the film (point 5). Table 4.1 shows the values for one of the samples. The values were obtained from the following simple relation:

$$Homogeneity = \frac{Thickness_{point}}{Thickness_{centre}} \tag{4.1}$$

To understand the homogeneity across samples, average homogeneity was calculated from the nine measurements from one sample, which was then compiled for other samples.

Table 4.1: Homogeneity of one of the samples

Sample point	Thickness	Homogeneity
1	215.4	0.939
2	217.5	0.948
3	215.5	0.94
4	226.9	0.989
5	229.3	1
6	227.5	0.992
7	219.5	0.957
8	222	0.968
9	218.9	0.954

The centre point of the sample was used to normalize other values as it was the thickest point in most cases. For example, the sample shown in Figure 4.1 had an average homogeneity of 0.965. The process was repeated for 20 films, out of which 16 films showed an average homogeneity greater than 90%. The samples below this level were either processed at higher pressure (6 or 8 mbar) or higher power (30 W). Therefore, controlling the deposition homogeneity in these processing regimes is harder. The list of values for all films can be found in Appendix A. The depositions are, thus, considered homogenous and other measurements such as Raman and activation energy were done for only one point on the sample.

4.2. Crystallinity of films

The crystal structure of thin films in thin-film solar cells is crucial in determining their performance and efficiency. The crystal structure refers to the arrangement and orientation of atoms or molecules within the thin film material. The crystal structure affects the movement of charge carriers (electrons and holes) within the thin film. A well-ordered crystal structure with fewer defects and higher crystallinity facilitates efficient charge carrier transport, reducing losses due to recombination. Amorphous films are, thus, designed to be thinner when integrated into solar cells.

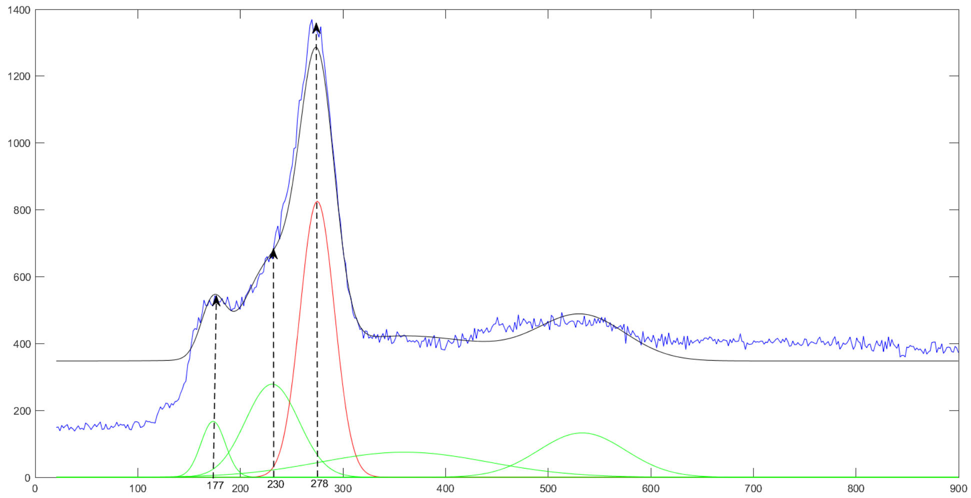

Figure 4.2: Fitted Raman spectrum for one of the samples showing the Gaussian peaks at various stretching modes

The structure has been identified using two different measurement techniques. Raman spectroscopy was performed for all samples to identify the intensity of vibration modes described in subsection 3.2.4. Figure 4.2 shows a typical spectrum obtained for amorphous samples. All the amorphous germanium stretching modes at 177 cm^{-1}, 230 cm^{-1} and 278 cm^{-1} are visible in the sample. The c-Ge peak at 300 cm^{-1} was not seen in any of the samples suggesting that the material is amorphous. The absence of this peak would also mean that the crystallinity value cannot be obtained for any of the samples. The amorphous nature of the material was also confirmed by the XRD measurement of one of the samples. Figure 4.3 shows no peaks corresponding to Ge crystal orientations at 27.15º, 45.30º and 53.65º were detected. Other samples have a similar Raman profile shape, leading to the assumption that all films are amorphous.

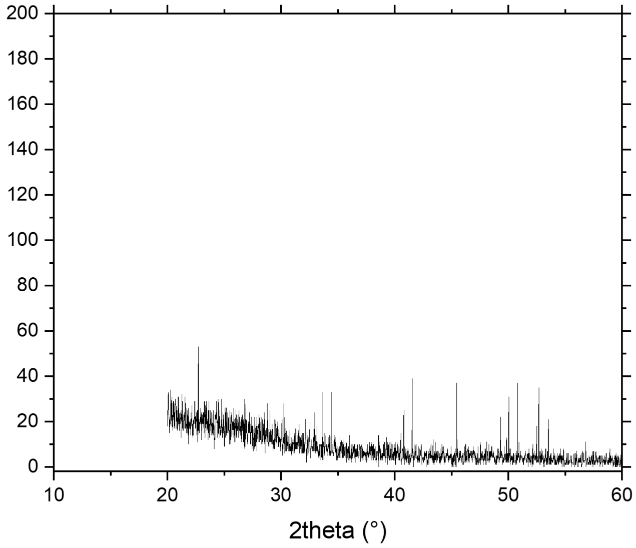

Figure 4.3: XRD measurement of one of the samples showing the absence of Ge crystal peaks

4.3. Bandgap approximation from RT measurements

The bandgaps presented later in this section have been extracted from the SE measurements. However, RT measurements can also determine the optical bandgap described as E_{opt}. The absorption spectrum of the material is calculated from reflection and transmission spectra. The bandgap corresponds to the minimum energy required for an electron to transition from the valence band to the conduction band, leading to an absorption edge in the spectrum. By analyzing the onset of absorption, the bandgap energy can be determined. This method has been used to cross-verify the bandgap values obtained from SE measurements.

The analysis performed for one of the samples is seen in Figure 4.4. The optical bandgap (E_{opt}) has been calculated using a MATLAB code shared in Appendix B. It interpolates data to obtain the point where the absorption is 0%. For this sample, the bandgap obtained from the absorption profile was 0.81 eV which was very close to the value obtained from SE measurements, i.e., 0.84 eV. Some samples did not reach the value of 0% absorption for the range of wavelengths measured. A linear fitting was performed for these samples to approximate the bandgap as shown in Figure 4.5. This approximation gave a value of 0.84 eV compared to 0.86 eV obtained from SE measurements for one of the samples.

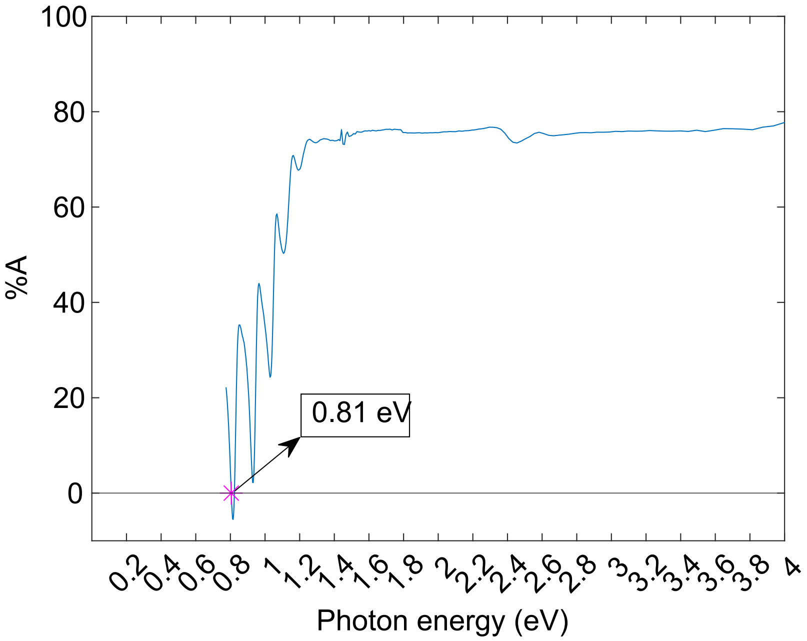

Figure 4.4: Absorption profile and approximation of bandgap at the onset of absorption

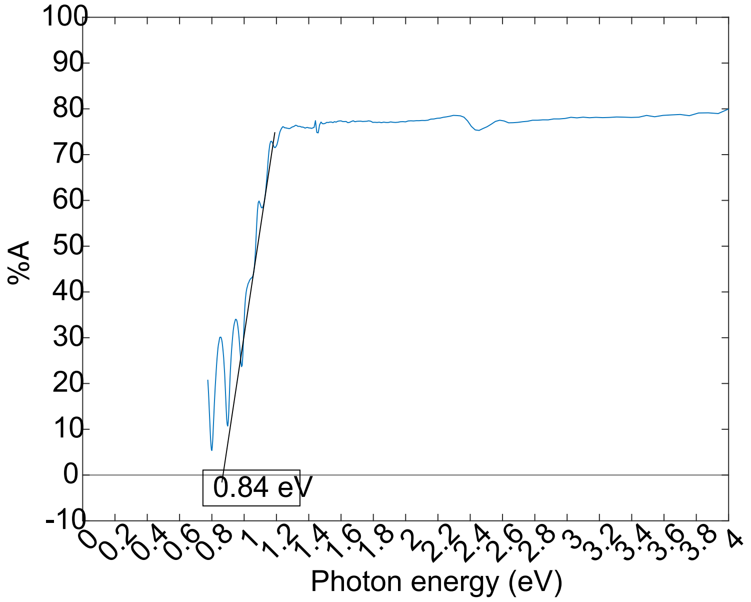

Figure 4.5: Absorption profile and extrapolation of bandgap by linear fitting

The percentage difference between the values for all samples can also be seen in Figure 4.6. This difference is calculated as:

$$\%difference = \frac{E_{opt} - E_{04}}{E_{opt}} \tag{4.2}$$

Please note that the absolute value of the difference is plotted. 22 out of all 30 samples produced have a value of less than 6%. Accordingly, it can be argued that the bandgap of the material is indeed in the range measured by both RT and SE measurements.

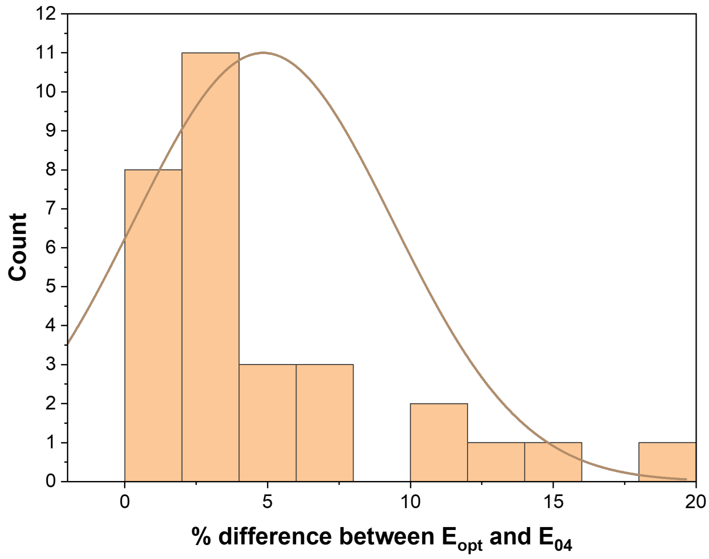

Figure 4.6: Histogram showing the distribution of % difference between E_{opt} and E_{04}

4.4. What are the suitable deposition conditions for intrinsic films?

As mentioned in subsection 3.1.1, several deposition parameters were varied to evaluate their effect on the film properties. The variations in key parameters such as refractive index, activation energy, the bandgap of materials etc, are covered. Deposition conditions that give the ideal film properties are covered. Finally, an ideal refractive index is discussed to corroborate some findings.

4.4.1. Effect of Power and Pressure

In the first series of deposition, both pressure and power were varied across nine samples. Other important parameters such as temperature, germane and hydrogen flows and deposition time were held constant. The substrate temperature was kept at 275 °C, and electrode distance was set at the lowest value possible by the equipment (13 mm), per findings from [57]. It was important to vary the pressure and power again to understand the effect of the showerhead configuration during PECVD. The values are listed in Table 4.2

Table 4.2: Deposition conditions for Pressure and Power variation series

Input Parameter	Value
Electrode gap	13 mm
Deposition Pressure (p)	4, 6 ,8 mbar
RF Power (P)	10, 20, 30 W
Germane flow Rate	2 sccm
H_2 flow rate	200 sccm
Substrate temperature	275 °C
Time	2000s

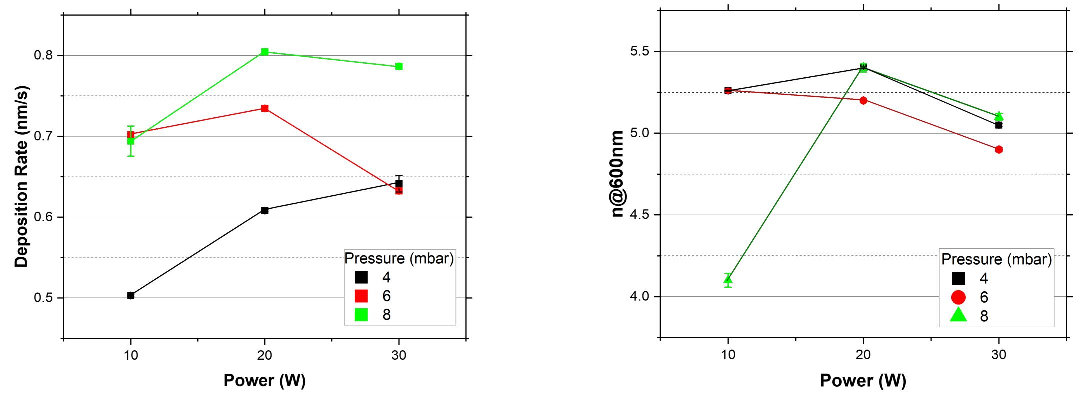

(a) Deposition Rate

(b) Refractive index @ 600nm

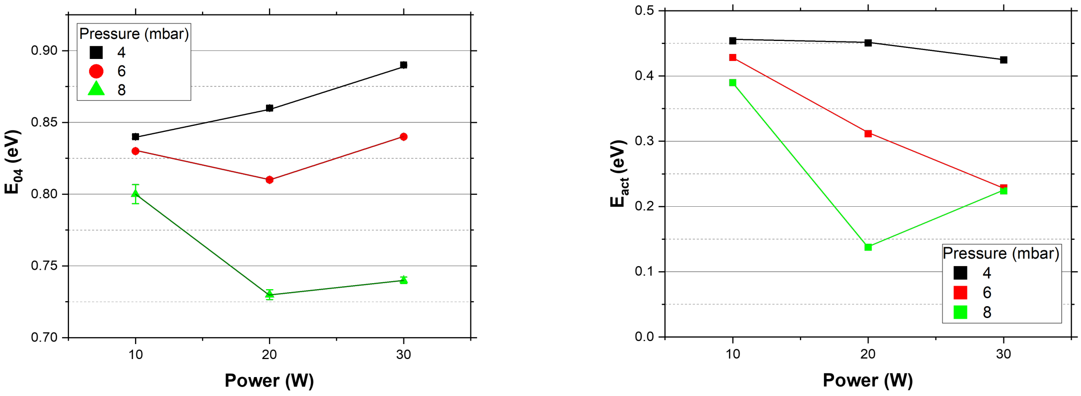

(c) Bandgap (E_{04})

(d) Activation Energy (E_{act})

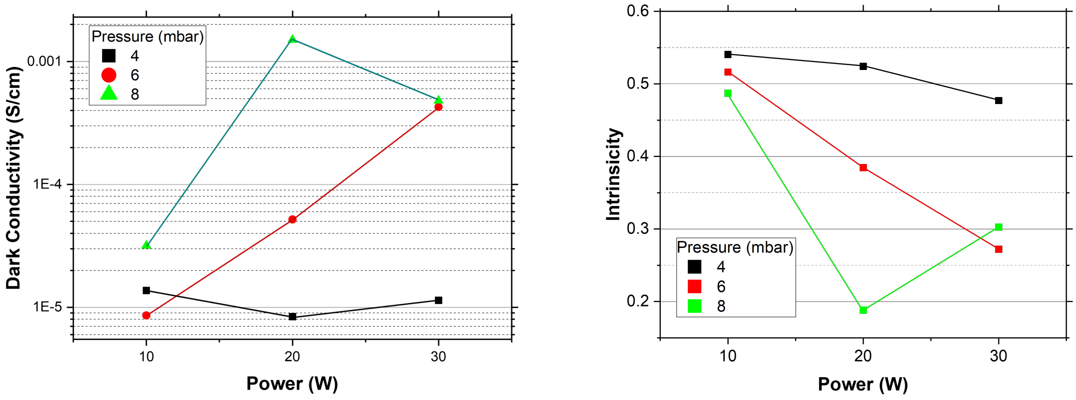

(e) Dark Conductivity

(f) Intrinsicity

Figure 4.7: Results showing the effect of power and pressure on material properties

Deposition rate has been presented instead of thickness to compare samples with different deposition times. The results shown in Figure 4.7a are inconclusive regarding the variation of the deposition rate ($\frac{deposition\ thickness}{deposition\ time}$) with power, but it was observed that all the films produced are over a micron thick under these conditions. More thickness-related data is covered in Appendix C. Moreover, pressure and power are observed to correlate positively with deposition rate, which agrees with literature [40]. As seen in Figure 4.7b, the refractive index is above 4.9 for all samples except one processed at a pressure of 8 mbar. Another important observation is the low activation energy seen in Figure 4.7d for samples processed at 8 mbar at higher power.

The other results presented in Figure 4.7 show that low pressure of 4 mbar gives more stable results regardless of power. Higher activation energy and lower dark conductivity are seen for all samples processed at a power of 10 W, resulting in high intrinsicity as seen in Figure 4.7f. It should also be noted that the intrinsicity seems to go below the ideal value of 0.5 for samples processed at higher power. This can be attributed to a lower deposition rate, leading to denser films with low defect density. Thus, the next batches of samples were processed at a power of **10W**. At lower pressures, the intrinsicity seems to be higher, and the material is also denser, with the trends more consistent. The pressure of 8 mbar was, thus, discontinued in the next depositions.

4.4.2. Effect of Pressure and Germane content

Based on the observations from the previous run, the next series of depositions fixed the power at 10 W. A pressure of 8 mbar is also not conducive to producing good films. Thus, the pressure was varied as 4 mbar, 5 mbar and 6 mbar. The deposition time was reduced from 2000 s to 500 s to obtain thinner films that were more representative of the films that would be used for the solar cell. Moreover, germane and hydrogen flow rates varied per values shown in Table 4.3. Higher germane content was explored in this series as it can affect the density and porosity of the material. An ideal germane content level with suitable material properties can, thus, be identified. With these settings, a total of 12 samples were produced. The rest of the conditions are the same as Table 4.2. Here, the germane content is calculated as:

$$GeH_4\ Content(\%) = \frac{GeH_4\ flow * 100}{GeH_4\ flow + H_2\ flow} \tag{4.3}$$

Table 4.3: Deposition conditions for Pressure and Germane Content series

GeH_4 Flow (sccm)	H_2 Flow (sccm)	GeH_4 Content (%)
200	2	0.99 (~1)
100	2	1.96 (~2)
100	8	7.41 (~8)
0	8	100

A clear relationship exists between germane content and deposition rate as seen in Figure 4.8a. With an exception for samples processed at a pressure of 5 mbar, the deposition rate increases with germane content. This could be attributed to the higher availability of germane radicals in the plasma or lower hydrogen etching in the film [57]. A higher deposition rate is undesirable as it allows for less control over the growth mechanisms of the films, impacting their reproducibility. Reproducibility is important if the material is used as a solar cell absorber layer in mass-produced solar cells. As seen in Figure 4.8b, the refractive index is lower for samples processed at high germane content of ~8% and 100%. It is relatively stable for samples processed at a pressure of 4 mbar. These observations point toward using low germane content for better films. This was also seen by Vrijer et al. [57]

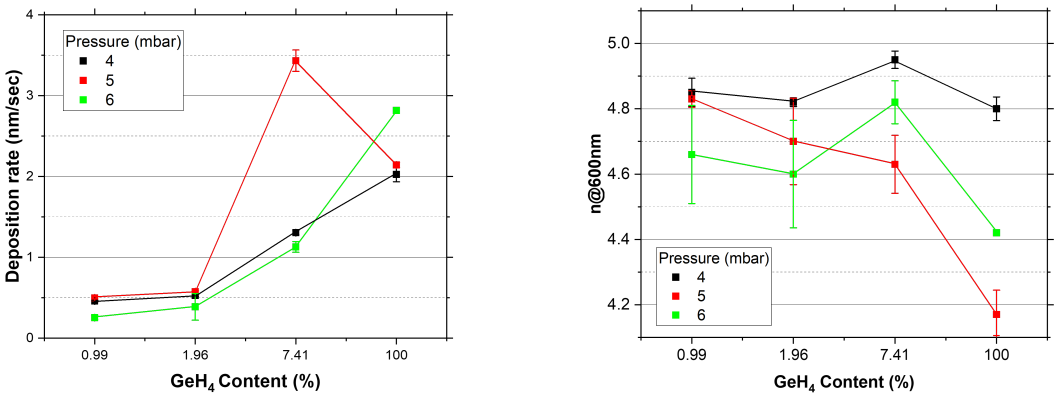

(a) Deposition Rate

(b) Refractive index @ 600nm

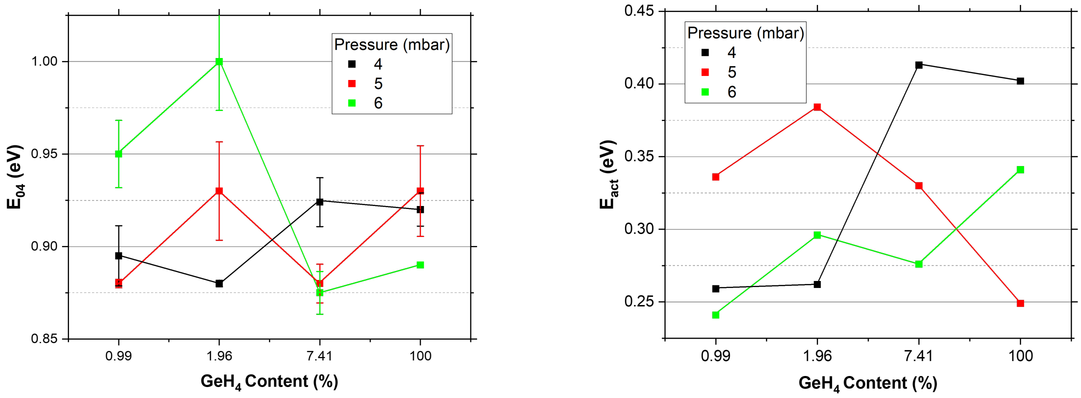

(c) Bandgap (E_{04})

(d) Activation Energy (E_{act})

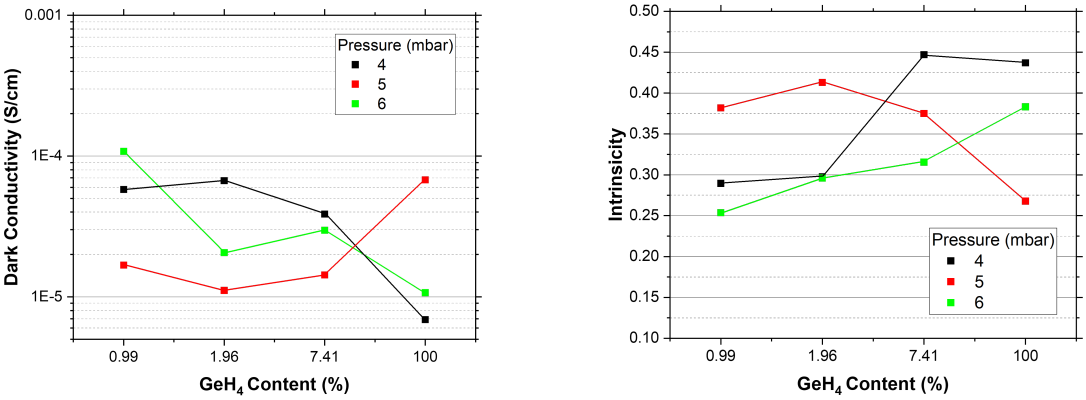

(e) Dark Conductivity

(f) Intrinsicity

Figure 4.8: Results showing the effect of germane content and pressure on material properties. The deposition time was reduced from 2000s to 500s

As for the effect of pressure, samples processed at a pressure of 6 mbar show a higher bandgap than other samples at low germane content, as seen in Figure 4.8c. Moreover, these samples do not achieve intrinsicity (Figure 4.8f) above 0.4, unlike the samples processed at lower pressures. Combining this with declining intrincisity seen at higher power from the previous batch makes this pressure an undesirable processing regime. Samples processed at a pressure of 4 mbar and 5 mbar show lesser variation in their bandgap when compared to samples processed at 6 mbar. The highest intrinsicity and activation energy (Figure 4.8d) is still seen for samples processed at 4 mbar, albeit with higher germane content. Samples processed at 5 mbar seem to perform better than samples at 4 mbar in terms of E_{act} and dark conductivity but lose this advantage at higher germane content values. Further research could be done to fine-tune the optimum pressure in the 5 mbar or lower range. Moreover, more research into the optimum germane content was performed in this study. However, with the present results, the pressure of **4 mbar** is a sensible design choice for intrinsic material.

4.4.3. Effect of Temperature and Early Ignition

With the observations from the second series, a pressure of **4 mbar** was considered suitable for film properties. Nine samples were made in three sets in the last series of intrinsic depositions. The germane content was reduced further as a higher hydrogen concentration would reduce the defect density by passivating more dangling bonds, and it might be possible to hit the nano-crystalline regime, which would have a lower bandgap. A slow deposition rate should give more time for the crystals to develop. GeH_4 at ignition might lower the deposition rate even further and make it possible to control the growth and potential crystallization better. Lower temperatures were also explored in this experiment. Even though the literature shows that higher temperature gets better films, the application within a solar cell might be complex. The doped layers might be destroyed when exposed to high temperatures. The samples and deposition conditions are listed in Table 4.4. Pressure, Power and electrode distance were fixed at 4 mbar, 10 W and 13 mm, respectively.

Samples were deposited on two substrates: 10 cm x 2.5 cm corning gorilla glass slices and (100) oriented crystalline silicon half-wafers. Germanium was deposited on crystalline silicon wafers for FTIR characterization. FTIR characterization was done to look for the presence of oxygen.

Table 4.4: Deposition conditions for temperature and early ignition series. Germane content was also varied for these samples

H_2 Flow (sccm)	GeH_4 flow (sccm)	GeH_4 Content (%)	Temperature (°C)
200	1	0.49 (∼0.5)	225
200	2	0.99 (∼1)	
200	3	1.48 (∼1.5)	
200	1	0.49 (∼0.5)	275
200	2	0.99 (∼1)	
200	3	1.48 (∼1.5)	
200	1	0.49 (∼0.5)	275 - early ignition
200	2	0.99 (∼1)	
200	3	1.48 (∼1.5)	

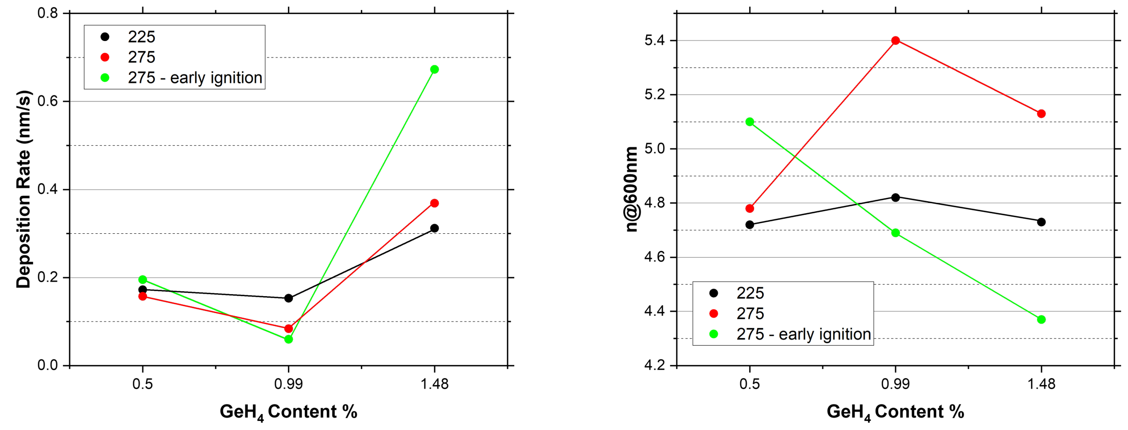

(a) Deposition Rate **(b)** Refractive index @ 600nm

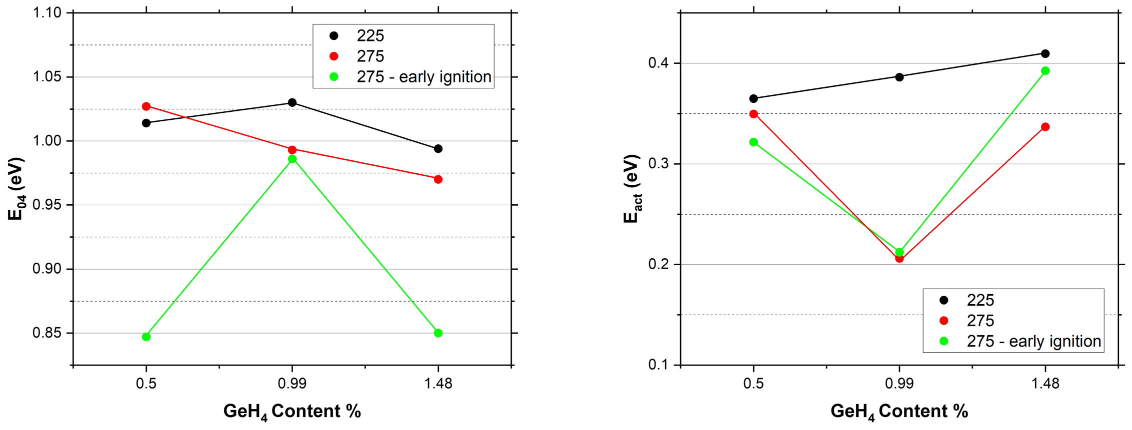

(c) Bandgap (E_{04}) **(d)** Activation Energy (E_{act})

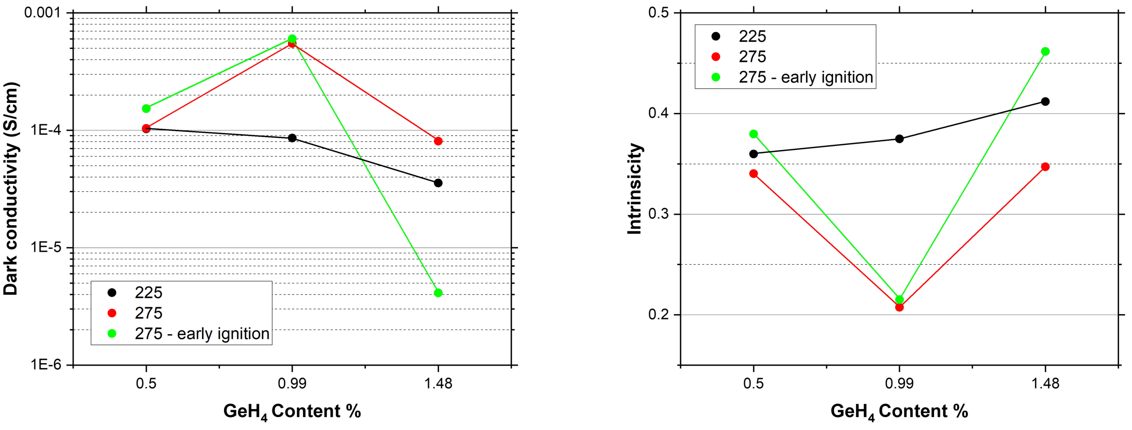

(e) Dark Conductivity **(f)** Intrinsicity

Figure 4.9: Results showing the effect of germane content, temperature and early ignition on material properties. Ignition was done after 10s of gas injection instead of 30 minutes.

As expected, samples with germane content of $\sim$1.5% show the highest deposition rates as seen in Figure 4.9a. Yet these samples have the lowest bandgaps, high activation energy, lowest dark conductivity and highest intrinsicity among all three categories. Samples deposited with $\sim$1% germane content showed an unusual decline in deposition rate compared to ones deposited at $\sim$0.5%. It may be due to instability in the plasma conditions, as this rate is much lower than seen in the previous samples. A lower deposition rate also leads to a higher density at both temperatures ignoring the effect of early ignition for samples processed at $\sim$1% germane content as seen in Figure 4.9b.

To look at the effect of temperature, samples deposited at 225 °C have a lower refractive index than those at 275 °C, ignoring the effect of early ignition. This is in line with results seen by Vrijer et al. ([57]), where it is argued that a higher substrate temperature facilitates denser films. Also, these samples perform better in activation energy, dark conductivity and intrinsicity. The effect on bandgap is inconclusive.

As for the effect of early ignition, the sample processed at $\sim$1.5% germane content has shown better material properties in terms of bandgap, activation energy and intrinsicity. A higher deposition rate is seen for $\sim$1.5% and $\sim$0.5% germane content. The density from refractive index measurements does not reflect the expected decreasing density pattern as the sample processed with $\sim$0.5% germane content shows a rise in refractive index. Other properties, such as activation energy and dark conductivity, also show inconclusive trends. The inconsistency in results can be attributed to instability in plasma conditions at low germane concentrations. GeH_4 dissociates faster than what is fed into the chamber, and the role of H_2 dilution is to prevent gas phase polymerization [46]. Low germane content assists in achieving a uniform plasma with lesser polymerized groups such as Ge_2H_6 and Ge_3H_8. Still, early ignition can lead to poor intermixing of gases, resulting in an unstable plasma. It is possible to achieve good films with this setting, but more depositions are required to confirm the reproducibility of films. Since the bandgap and intrinsicity improve for all samples, germane content of 1-1.5% can be explored in depositing cells.

4.4.4. Ideal Density of films

The refractive index has been used as a metric to understand the density of the amorphous tissue. The plots of other parameters with the refractive index can be used to identify the ideal material properties to watch for when depositing intrinsic films. Since the film is to be used as a low bandgap material, the plots of bandgap (E_{04}), activation energy (E_{act}) and intrinsicity can be observed in the figures.

The effect of pressure on both the refractive index and the bandgap of the films is seen in Figure 4.10. The bandgap decreases with the refractive index for films processed at the same deposition pressure. So, the bandgap goes down if the films have a higher density at the same deposition pressure. At the same time, the bandgap goes up with decreasing pressure which explains the overall rising trend. The rise of bandgap with decreasing pressure may come from the decreasing size of the individual amorphous structures as the material becomes more dense [1]. As these structures reach a nanosize, it can lead to quantum confinement that can increase the band energy of each structure. More analysis needs to be performed to confirm if this is the case. Density Function Theory calculations with Hybrid Functional (HSE06), as performed by Abdullah in [1], can be repeated for germanium to confirm if this is the case. It requires determining the dislocation density and size of the nanostructures, which can be obtained from Transmission Electron Microscope (TEM) measurements.

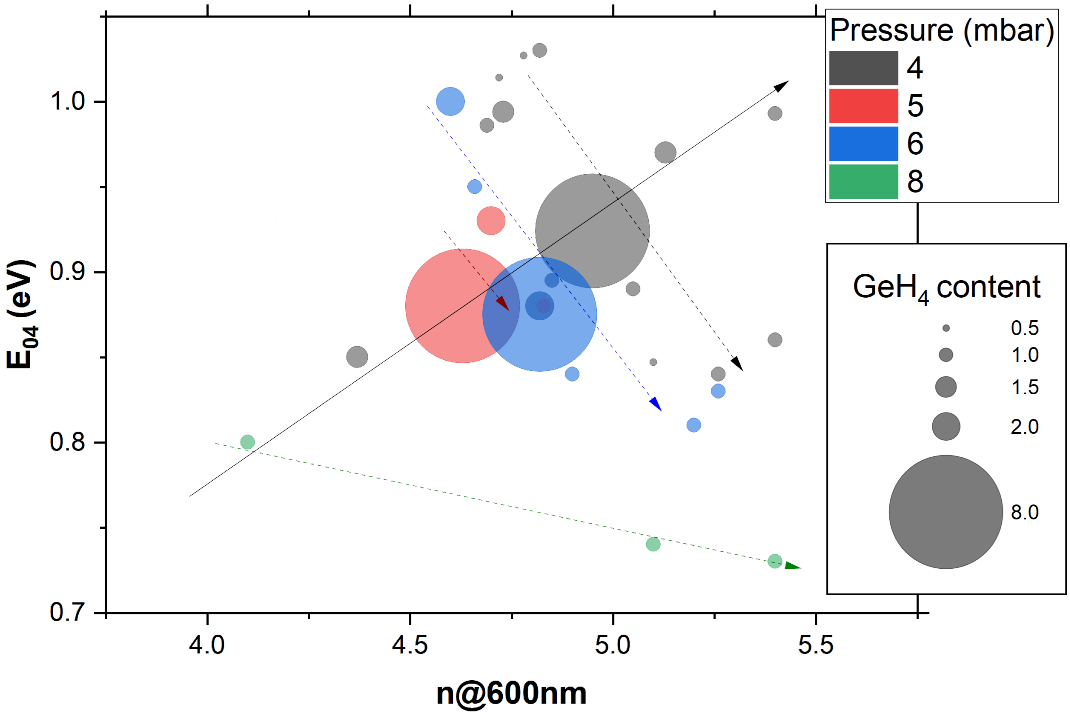

Figure 4.10: Plot showing the bandgap (E_{04}) varying with refractive index

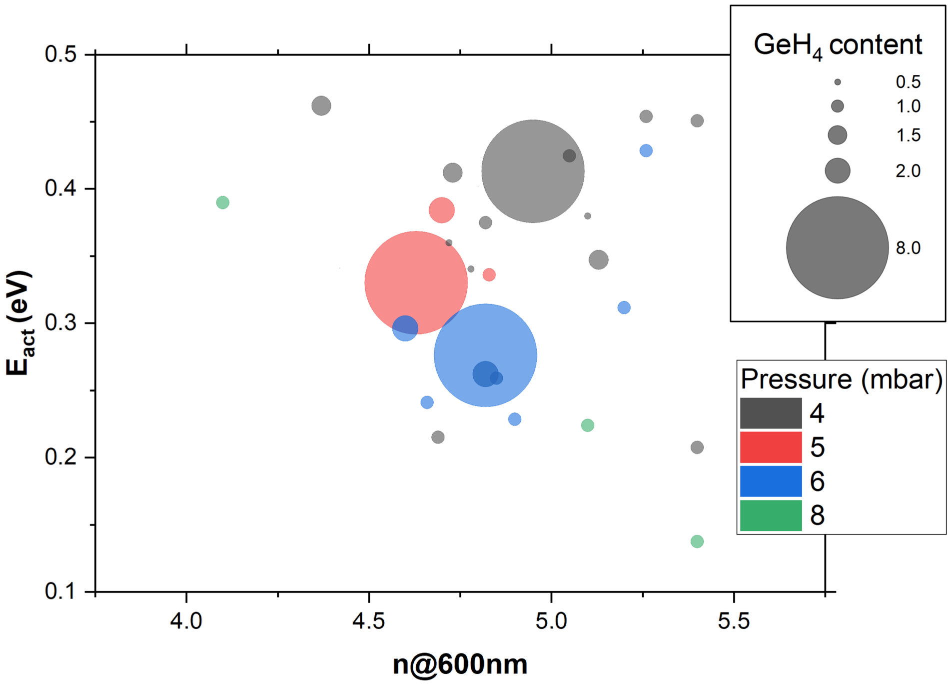

Figure 4.11: Plot showing the bandgap (E_{act}) varying with refractive index

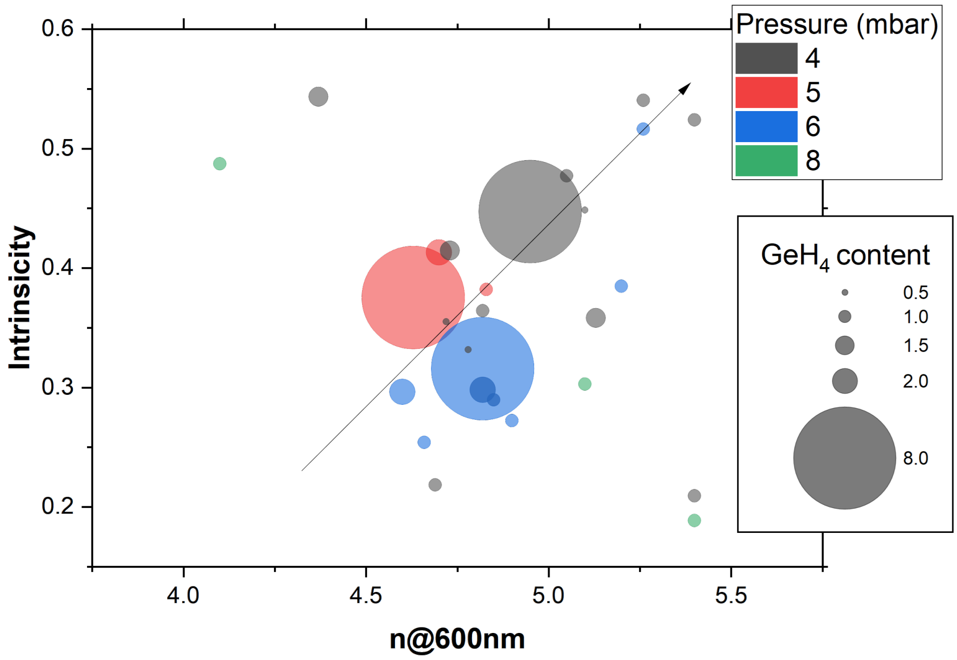

Figure 4.12: Plot showing the intrinsicity (E_{04}) varying with refractive index

The activation energy (Figure 4.11) also increases with pressure. The effect of the refractive index on the activation energy is inconclusive, but a higher variation is seen at the refractive index higher than 5. Moreover, intrinsicity (Figure 4.12) increases with the refractive index. This means that denser materials can achieve higher activation energy and intrinsicity, which is probably because denser materials are closer to the crystalline phase and can have fewer defects such as voids in the lattice. In such a case, one can find a sweet spot of refractive index between 4.7-4.9 where the bandgap is not too high and intrinsicity and activation energy is not too low. These values are obtained when the pressure is between 4-5 mbar, germane content is between 1-2%, and power is 10W. The temperature range from 225 °C to 275 °C was also observed to give these results.

4.5. Stability expermients

These sets of experiments were performed to understand the degradation in properties of the intrinsic films when exposed to environmental factors. Two types of degradation are studied: light-induced degradation and oxidation in air. The results for each are presented as follows.

4.5.1. Oxidation in air

As soon as the films are deposited, they are kept in a vacuum chamber to prevent post-deposition oxidation. Oxidation can lead to the growth of the GeO_x layer as Ge dangling bonds react with oxygen molecules in the air. Oxidation induces defect states in the lattice with energy close to the conduction band [57]. Thus, it can result in the degradation of activation energy. Oxidation has been monitored for two sets of samples in separate experiments using two different techniques. Both techniques look for oxygen signatures.

Seven samples were selected for the first study. These samples were taken from the first and second series of depositions and were all processed at a pressure of 4 mbar. The pressure of 4 mbar was chosen for these films as it was identified as an ideal processing regime. Samples from the first series were processed with different RF power settings, i.e. 10 W, 20 W and 30 W. Samples from the second series were processed with germane content of 0.5%, 1%, 1.5% and 8%. No samples were selected from the third series, as the study was performed before these depositions.

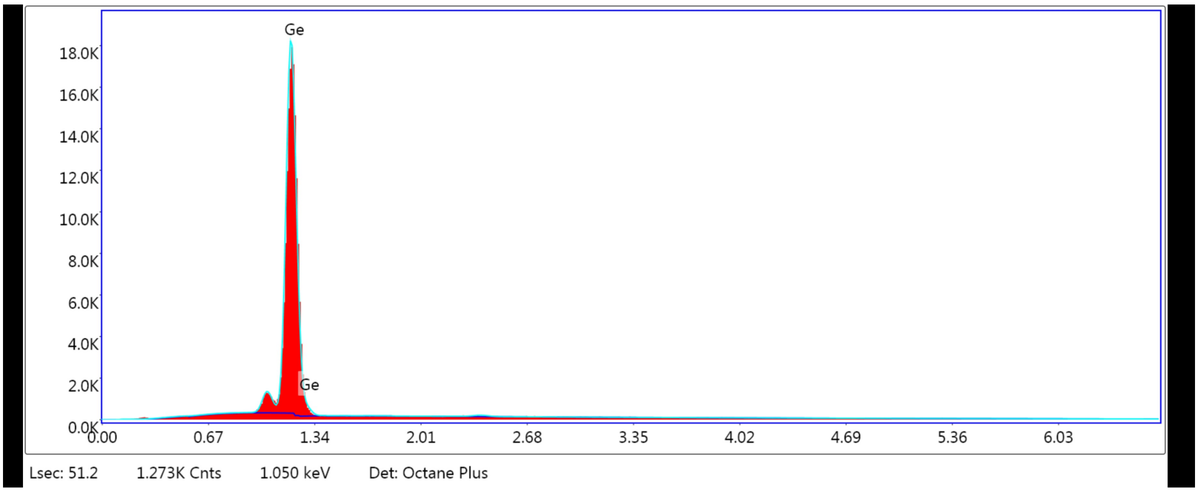

(a) Sample before exposure

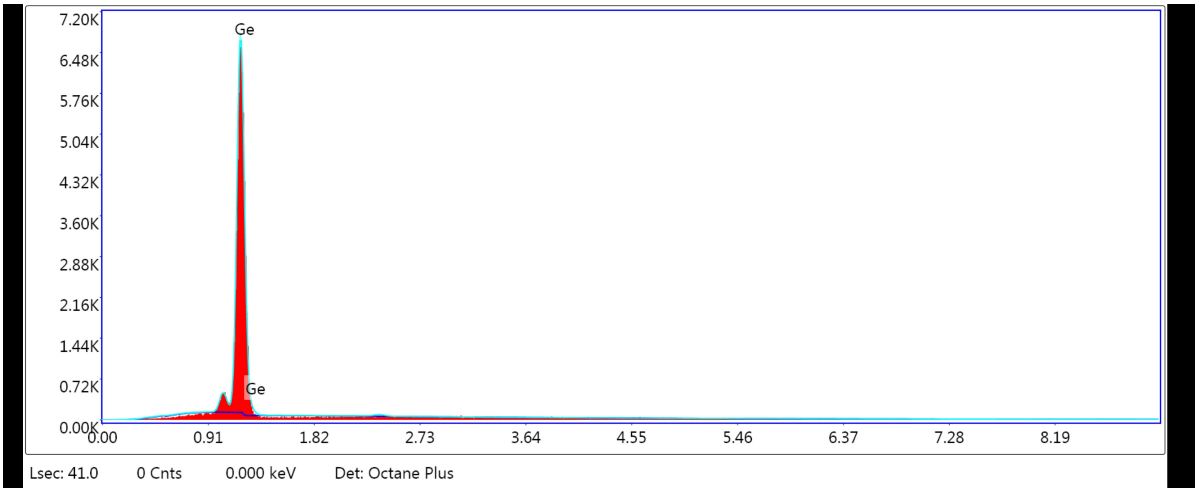

(b) Sample measured after two months

Figure 4.13: Results of EDX testing for one of the samples. This sample was processed at a power of 10 W and germane content of 0.99%

EDX measurements for these samples were performed right after removing them from the vacuum chamber to understand the initial elemental composition. Samples were then exposed to air in an indoor environment for two months, following which EDX measurement was done again to see any change in composition. The result for one of the samples can be seen in Figure 4.13. The spectrum shows absolutely no change in elemental composition. The ratio of large Ge peak to small peak was ten initially (18K/1.8K) and stayed the same after two months (7.2K/0.72). Four more samples were similarly exposed and measured and showed a similar trend where no significant rise in oxygen signature was detected. Results for these samples can be found in Appendix D.

The second set of samples was picked from the last run of depositions, where the films were deposited on crystalline silicon substrates. FTIR measurements were performed on the films after deposition and after two weeks of indoor air exposure. The fitted FTIR spectra for three samples are shown in Figure 4.14. Samples are chosen from each of the three temperature settings, i.e., 225 °C, 275 °C, and 275 °C but with early ignition.

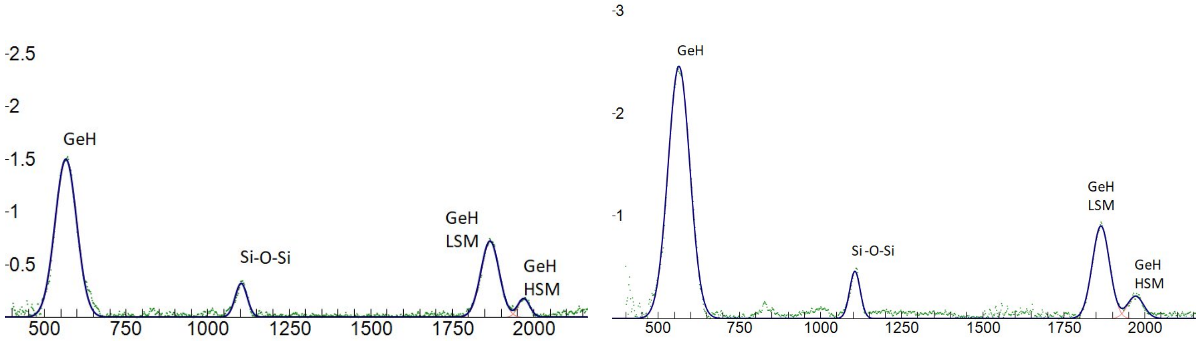

(a) Sample processed at 225 °C after deposition **(b)** Sample processed at 225 °C measured after two weeks

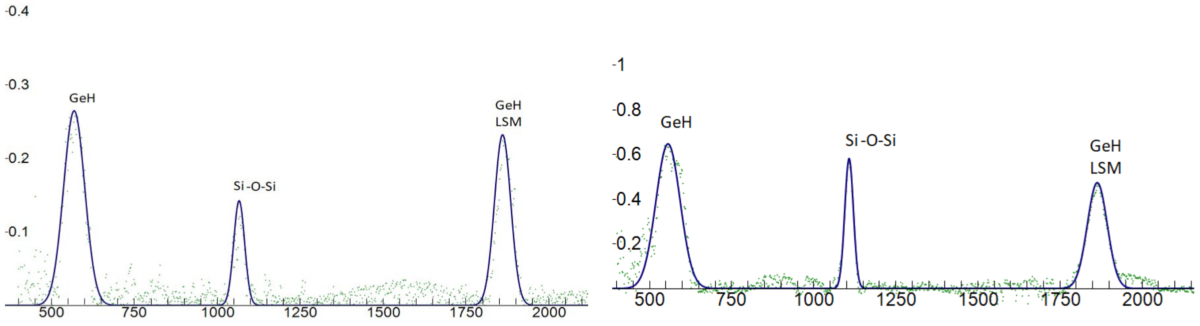

(c) Sample processed at 275 °C after deposition **(d)** Sample processed at 275 °C measured after two weeks

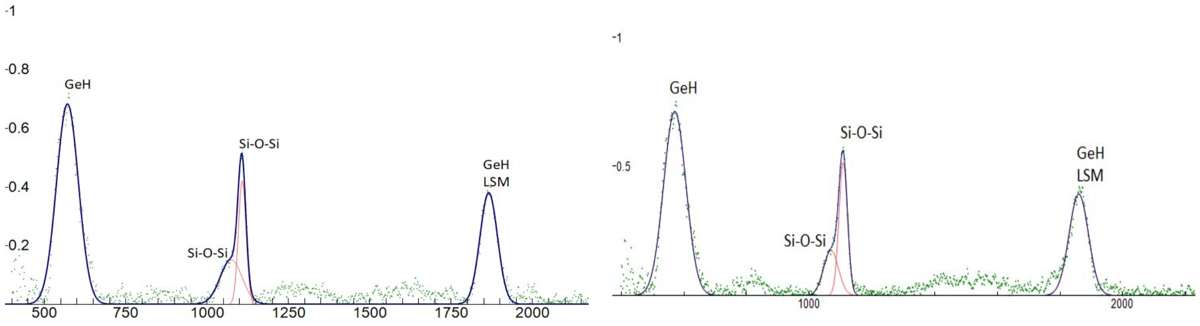

(e) Sample processed at 275 °C with early ignition after deposition **(f)** Sample processed at 275 °C with early ignition measured after two weeks

Figure 4.14: Results of FTIR measurements for selected samples deposition and after two weeks exposure

FTIR spectrum of sample processed at 225 °C shows the presence of Ge:H stretching modes located at 560 cm^{-1}, 1875 cm^{-1} and 1980 cm^{-1}. The high stretching mode (HSM) located at 1980 cm^{-1} is missing for the other two samples deposited at 275 °C. These samples are less porous since HSM occurs at GeH bonds present at nanosized pores [56]. The peak visible around 1100 cm^{-1} refers to the SiO$_x$ stretching mode coming from the substrate. This peak shows an additional SiO$_x$ stretching mode for the Sample processed at 275 °C with early ignition, which was only 96 nm thick. It was deposited at the lowest germane content of 0.5%. No sign of GeO$_x$ peaks seen in Figure 3.7 at 860 cm^{-1} is observed in any of the samples. Also, the difference in the relative size of peaks for the sample processed at 275 °C may be attributed to the weak FTIR signature of the sample in its first measurement.

4.5.2. Light-Induced Degradation

It is commonly known that light affects the performance of solar cells. Light-Induced Degradation (LID) in hydrogenated a-Si, also known as the Staebler-Wronski effect, was discovered in 1977 [52]. The efficiency of solar cells degrades within the first few hours of light exposure due to the creation of metastable defects on the a-Si layer. Although this effect is studied in cells, observing its effect on hydrogenated germanium thin films deposited in this research can give important insights into its use as an absorber material. Samples for this study were the same as the ones used for the oxidation study via EDX.

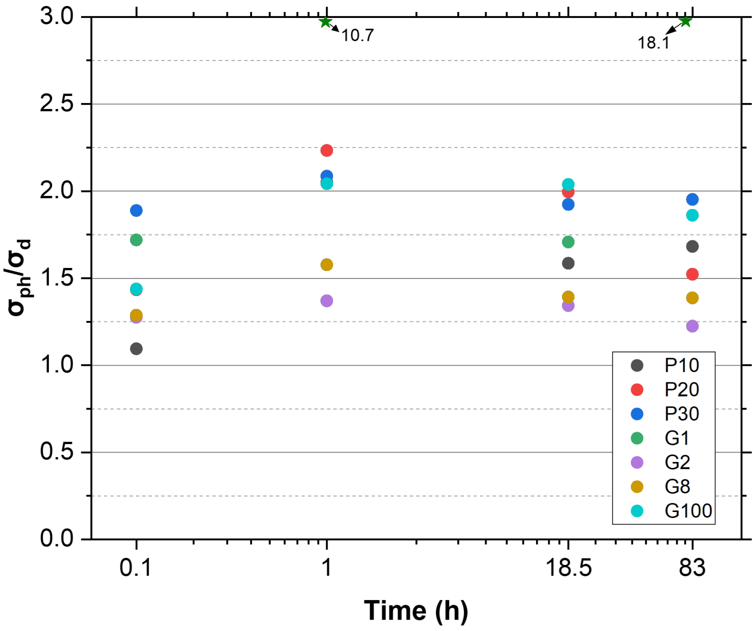

Figure 4.15: Plot showing the photoresponse of films with time

The thin films were exposed to a light source of $700 W/m^2$ that mimicked the AM1.5 spectrum at a stage temperature setting of 50 °C for multiple time intervals, namely 0 hr (no light soaking), 1 hr, 18.5 hrs and 83 hrs. Dark conductivity, activation energy and photoconductivity were measured at each interval per the procedure described in subsection 3.2.3. The ratio of σ_{ph} and σ_d, also known as the photoresponse, is also calculated to understand the effect on photoconductivity irrespective of changes in dark conductivity. The plot showing the evolution of photoresponse with time can be seen in Figure 4.15. For the labelling of samples, P denotes power, and G denotes the germane content, followed by the value of the condition. All samples from the power (P) series were processed at a germane content of $\sim$1%, and all from the germane (G) content series were processed at a power of 10 W. Sample G1 showed outlier values. In contrast, all other samples were observed to have values between 1% and 2.4%.

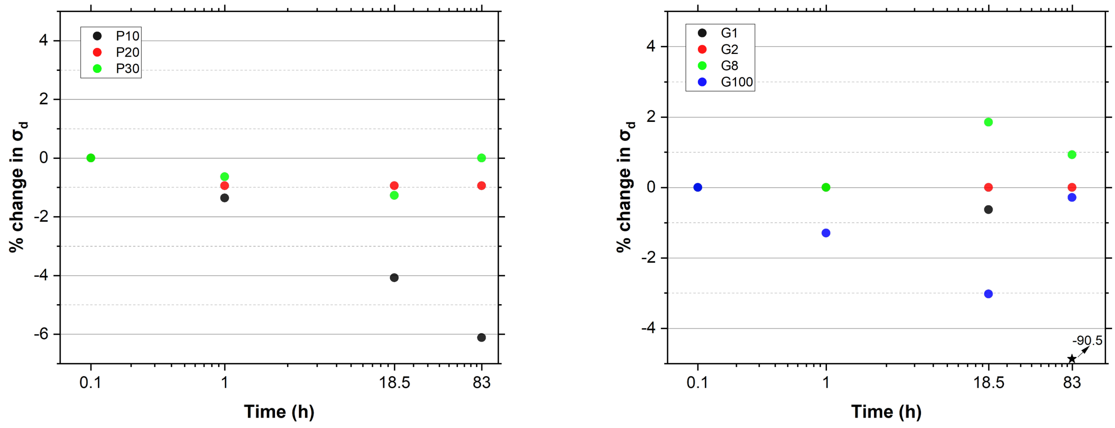

(a) % Change in Dark Conductivity for power series

(b) % Change in Dark Conductivity for germane series

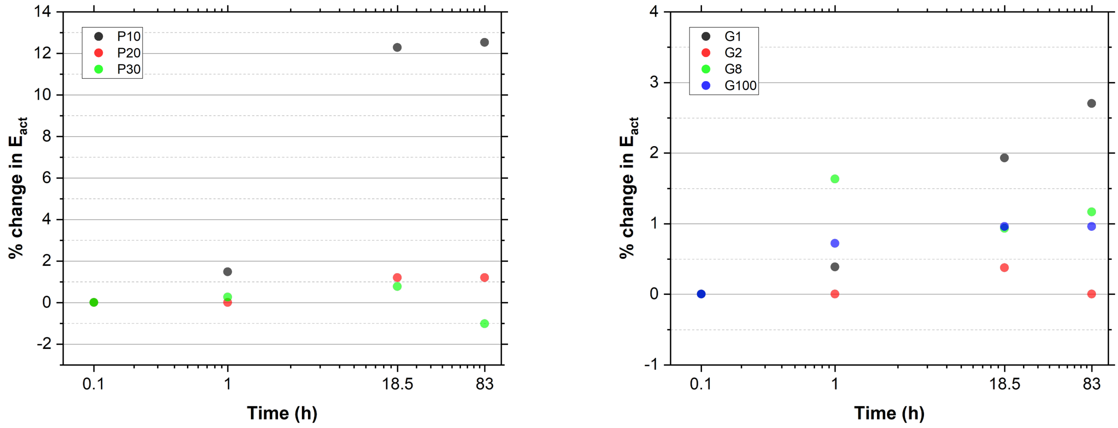

(c) % Change in E_{act} for power series

(d) % Change in E_{act} for germane series

Figure 4.16: Evolution of dark conductivity and activation energy after LID testing for selected samples (Note that the results are plotted from a value of 0.1 instead 0h on the x-axis due to a logarithmic scale)

To compare the changes over time, % change in each value is plotted in Figure 4.16 and Figure 4.17. The samples from power series and germane series samples are plotted side-by-side. Figure 4.16 shows that all samples, except one, deviate less than 3% from their initial values of dark conductivity and activation energy. This extra shift can be attributed to measurement error and may not reflect any physical phenomenon affecting the thin films. Moreover, most samples show an improvement in these properties where dark conductivity decreases and activation energy increases. This decrease in dark conductivity can be attributed to several factors. It typically indicates a decrease in the mobility of electrons or holes or a modification in the distribution of defect densities within the bandgap [22].

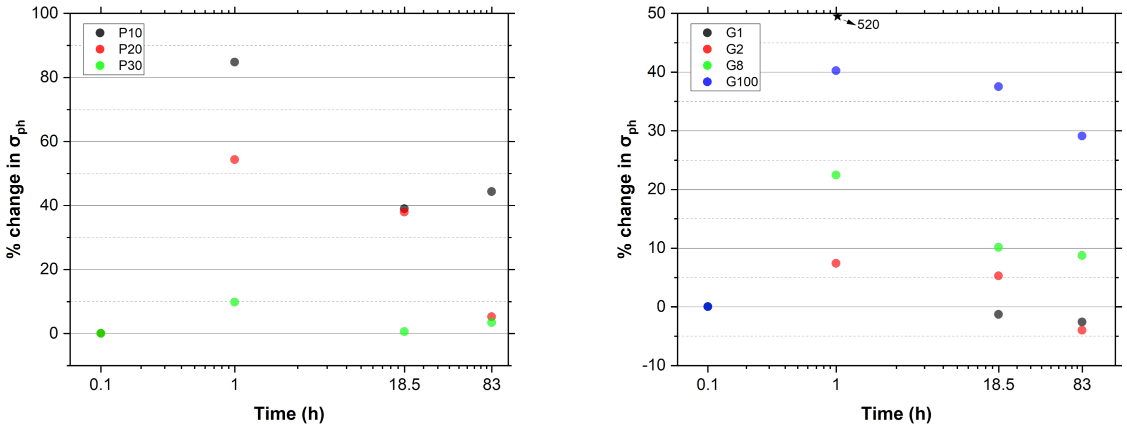

(a) % Change in photoconductivity for power series **(b)** % Change in photoconductivity for germane series

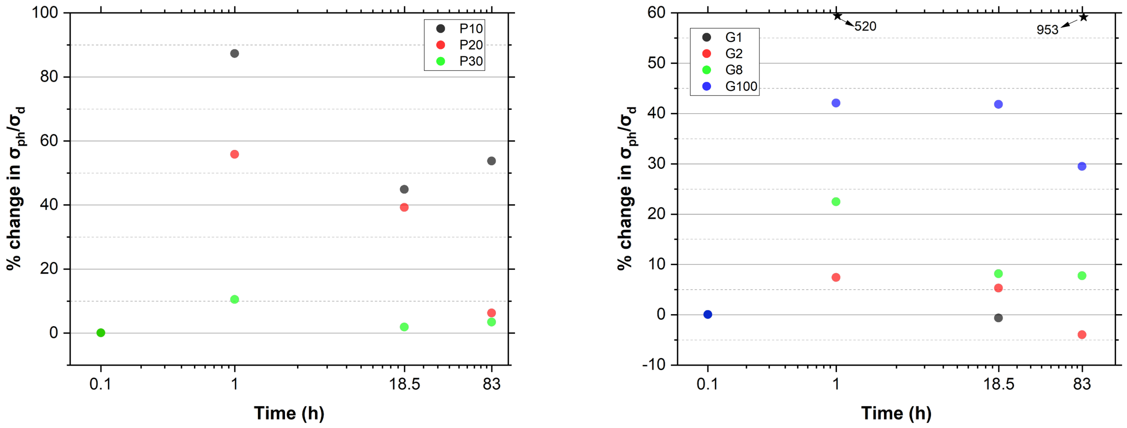

(c) % Change in Photoresponse for power series **(d)** % Change in Photoresponse for germane series

Figure 4.17: Evolution of photoconductivity and photoresponse after LID testing for selected samples (Note that the results are plotted from a value of 0.1 instead 0h on the x-axis due to a logarithmic scale)

The photoconductivity of all films increases after the first hour of light soaking. So the decrease in mobility of charge carriers can be ruled out. However, this effect is reduced with time. Perhaps, there is an initial rearrangement of defect states caused by fast switching between thermal/light generation and recombination of charge carriers. The reason can be attributed to the low bandgap and the high absorption coefficient of germanium compared to amorphous silicon, where this effect is not observed. Photoresponse also follows σ_{ph} as there is limited change in σ_d. The results show very little degradation in the photoresponse of the films for the duration of soaking. If there is an initial rearrangement of defect states due to annealing, the samples are seen to degrade with time. If this experiment is continued for a longer period, degradation from initial values may be observed.

4.6. Discussion

4.6.1. How intrinsic is the material?

The material is considered intrinsic if the activation energy lies in the middle of the bandgap. Thus, the value of intrinsicity should be close to 0.5. Figure 4.18 shows the variation of activation energy with bandgap with a trendline denoting the target value for the films. 7 of the 16 samples processed at 4 mbar lie close to the trendline. Other pressure conditions do not show this consistency, thus, supporting the processing condition chosen for the depositions. The list of bandgap, activation energy and intrinsicity values for all samples can be found in Appendix E.

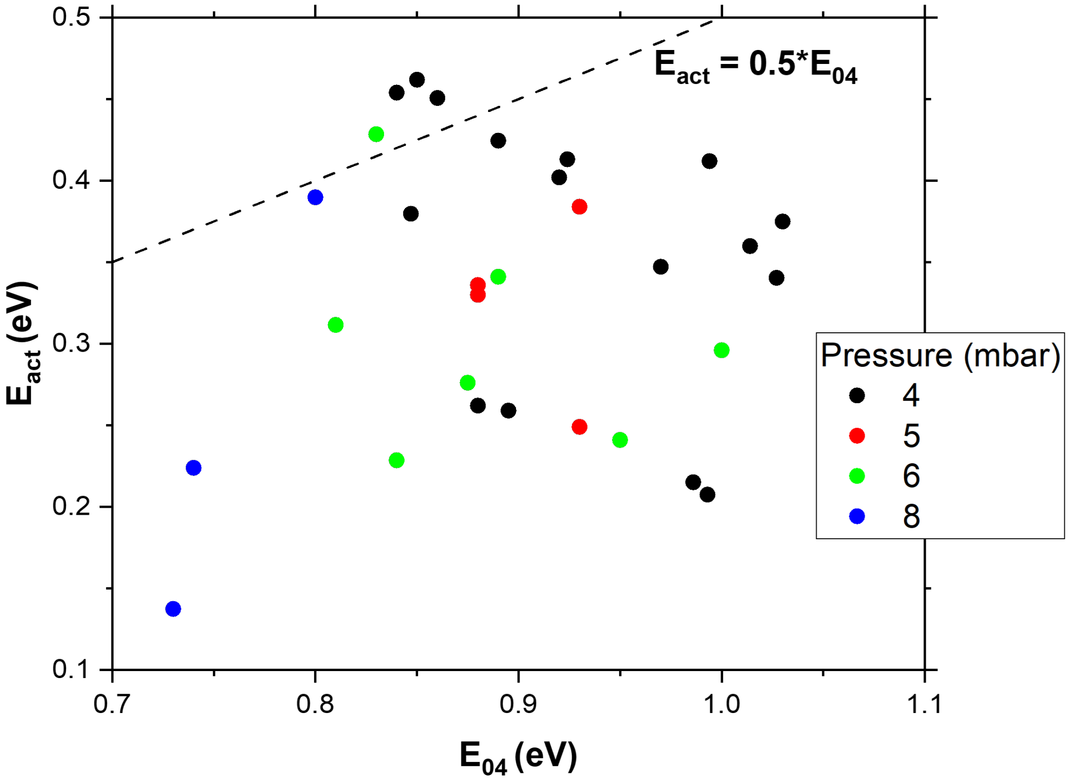

Figure 4.18: Plot showing the Activation energy (E_{act}) varying with Bandgap (E_{04})

4.6.2. What was the effect of using the showerhead configuration?

Previous research in the group [57] had produced numerous films which were deposited in a direct PECVD reactor. This research started with the hypothesis that a showerhead PECVD configuration can improve the properties of the deposited films. To verify the hypothesis, the samples are compared to previous results and are presented in the following figures.

Figure 4.19 shows the distribution of activation energy with the bandgap of the material along with the trendline representing the target intrinsicity of the samples. The green dots are the new Ge films developed during this research. These films are observed to have a much lower bandgap and higher activation energy than the Ge films deposited previously (black dots). The dots are also closer to the trendline showing that the samples are more intrinsic. The average bandgap of the samples from one set to the other goes down by roughly 36%.

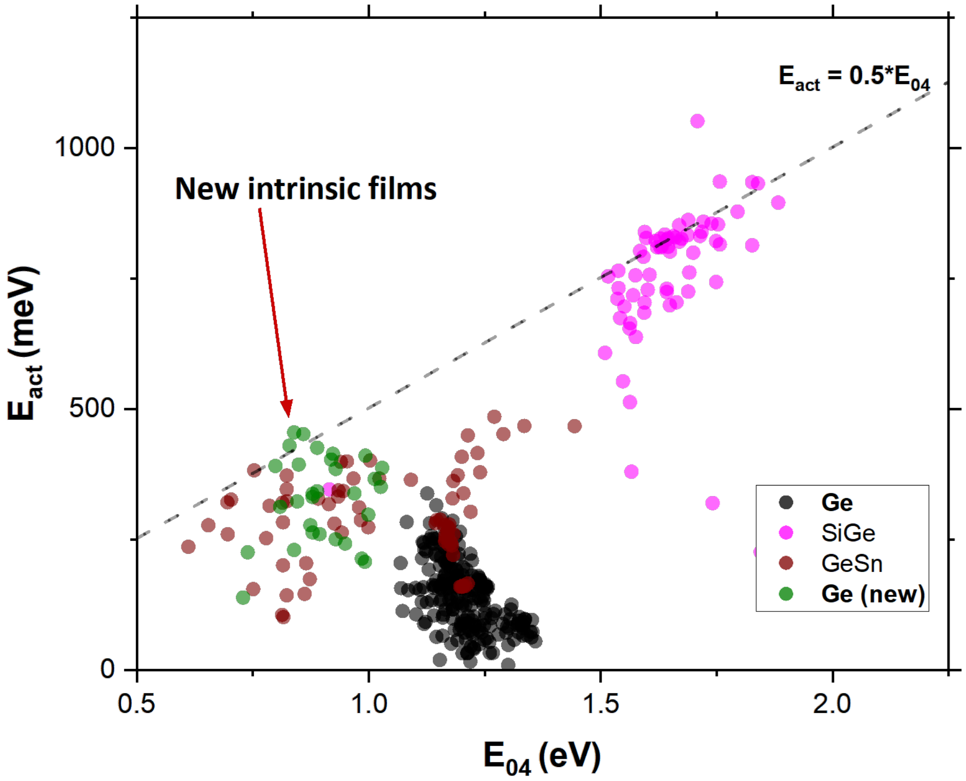

Figure 4.19: Plot showing the Activation energy (E_{act}) varying with Bandgap (E_{04}). Data is obtained from this research and [57]

The increase in average activation energy from the previous Ge batch is roughly 50%. An improvement in activation energy can be attributed to the absence of an oxygen signature that can introduce defect states which are more n-type [57].

This suggests that the showerhead configuration has led to lower porosity in the samples as oxygen occupies the sites with larger pores. The showerhead configuration may have affected the reactivity of Ge-radicals and the consequent growth of the film. Since germane dissociates more freely and has a higher reactivity when compared to silane [46], the surface mobility of germane is expected to be lower [5]. Vrijer et al. [57] had argued that void integration in the film might be surface diffusion controlled similar to that observed in amorphous silicon [48]. Thus, the surface mobility of Ge-radicals must have increased due to showerhead injection as gases are injected close to the substrate with a higher speed due to distributed flow from showerhead pinholes. Ge-radicals can travel more freely and require lesser activation energy to reach a site which would otherwise be void. The threshold temperature observed by Vrijer et al. [57] above which films were dense enough to prevent post-deposition oxidation could have come down as seen from the FTIR results of temperature in subsection 4.5.1

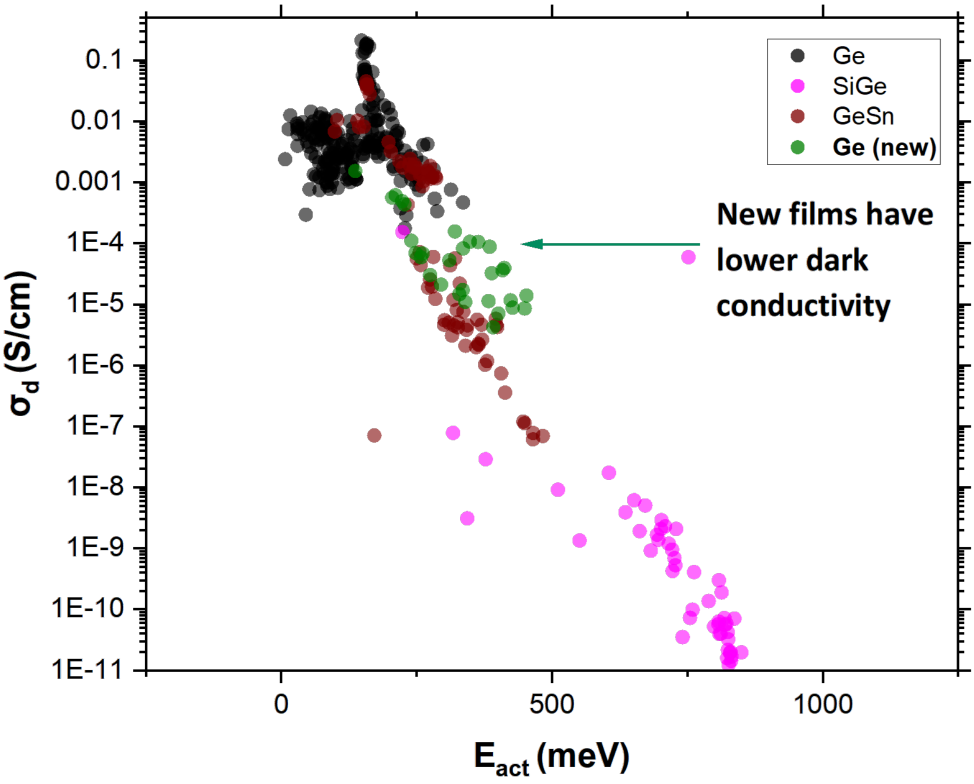

Figure 4.20: Plot showing the Dark conductivity (σ_d) varying with activation energy (E_{act}). Data is obtained from this research and [57]

Variation of dark conductivity with activation energy is seen for all the samples in Figure 4.20. Dark conductivity is known to go down with rising activation energy for various semiconductors [51] [23]. This is also seen in the new Ge films (green dots) deposited in this research compared to previously deposited germanium films (black dots) [57]. Lower dark conductivity confirms the fact that the activation energy of the samples is higher than before. The two figures also show that intrinsic Ge films can be obtained without Sn precursor. This simplifies the development of a low-bandgap material that can be processed without a complex amalgamation of raw materials and fewer variables to keep track of.

5

Conclusion

The aim of this research was to process and characterize hydrogenated germanium films to use them as a low bandgap intrinsic absorber layer for p-i-n structure solar cells. The films were deposited using PECVD. Three research questions were defined at the beginning of this research. These are answered one by one.

What are the deposition conditions for obtaining intrinsic germanium films?

Investigation of parameter space for PECVD depositions was done by depositing 30 films to find the optimum conditions for obtaining intrinsic films. All the films produced were amorphous in nature. The conditions varied were power, pressure, germane to hydrogen flow ratios, deposition time, substrate temperature and ignition time of the plasma to the introduction of gases. It was found that dense intrinsic films are obtained at a pressure of **4 mbar**, power of **10W** and germane to hydrogen flow ratio of **1-1.5%**. Higher pressure and power resulted in inconsistent or poor activation energy and bandgap results. Refractive index in the range of 4.7-4.9 was observed for most films deposited at these conditions.

What is the influence of exposure to air and light on the films?

When the samples are exposed to air, films could develop an oxide layer which is detrimental to material properties such as activation energy. EdX measurements were performed on films after two months of exposure following which no oxygen signature was detected. Moreover, some films were also monitored using FTIR which can detect any Ge-O vibration. No sign of oxygen was detected for these samples after two weeks of air exposure.

The film was also exposed to light for a total of over 80 hours. Dark conductivity was observed to reduce with exposure and photoresponse showed an initial rise followed by a declining trend. The initial jump in the first hour could be due to the rearrangement of defect states due to annealing. For the duration of exposure, photoconductivity did not degrade below the initial value. Since degradtion observed under Staebler-Wronski effect is generally highest in the first 10 hours of lightsoaking, material is not expected degrade significantly if this duration is further increased.

Has the showerhead PECVD configuration helped in improving film quality?

Previous research had deposited Ge:H films using a direct PECVD reactor. It was hypothesized that a showerhead configuration in the reactor can lead to better control of reaction mechanics giving films with desired material properties. After comparing the films with the previous depositions, it was found that some of the new films were indeed intrinsic. The films are observed to have a lower bandgap and higher activation energy than the previous Ge films. An improvement in activation energy can be attributed to the absence of an oxygen signature that can introduce defect states which are more n-type.

The research has, thus, proven its objective of producing intrinsic hydrogenated germanium films. The layer can be used as an intrinsic layer in a p-i-n structure device, paving the way for a new generation of high-efficiency solar PV devices.

6

Recommendations

The research has demonstrated the procedure to produce and characterize intrinsic hydrogenated germanium films. However, several steps in the process could be improved for better characterization and processing of films, making them suitable as low bandgap material. The recommendations for future research are covered in this chapter.

Firstly, some parameters in the processing could be explored further to optimize the film properties. Samples processed at a pressure of 5 mbar also showed the potential to be a low bandgap material. These samples had a lower bandgap, albeit with higher activation energy. The pressure range can be explored between 4-5 mbar in future research. Another parameter that can be explored is the germane content. Low germane content levels of 1% resulted in an unstable plasma in the last series. To obtain reproducible results, it is recommended that more samples could be made with germane content in the range of 1-2%. The effect of early ignition of plasma on the film properties shows potential, but more samples should be made to understand the effect with certainty.

Secondly, the photoconductivity of the films was found to improve and then degrade under exposure to light. Although the films were not found to degrade below the initial levels, the effect of long-term exposure cannot be ruled out. Future studies should expose the films for more than 100 hours to understand the effect completely. Regarding the oxidation experiment, samples can be exposed to DI water which has a stronger chance of oxidizing the films.

Thirdly, there were some issues in determining the crystallinity of the samples using Raman spectroscopy. Using XRD for the samples confirmed the structure of the material. More in-depth analysis can be performed on crystallinity at different conditions of depositions and exposure to environmental conditions.

Lastly, the bandgap of the films has been characterized optically, but the real application of the films lies in their integration in cells. Thus, future research should integrate the cells into p-i-n devices to test the performance in a single junction a-Ge solar cell. External Quantum Efficiency and Current-Voltage characteristics of the cell could quantify the electrical bandgap and potential collection of charge carriers.

References

[1] Botan Jawdat Abdullah. “Size effect of band gap in semiconductor nanocrystals and nanostructures from density functional theory within HSE06”. In: *Materials Science in Semiconductor Processing* 137 (2022), p. 106214. ISSN: 1369-8001. DOI: `https://doi.org/10.1016/j.mssp.2021.106214`. URL: `https://www.sciencedirect.com/science/article/pii/S1369800121005515`.

[2] Pablo Alfaro-Calderón, Mijail Cruz-Irisson, and Chien Wang-Chen. “Theory of Raman Scattering by Phonons in Germanium Nanostructures”. In: *Nanoscale Research Letters* 3.2 (2007), pp. 55–59. DOI: `10.1007/s11671-007-9114-0`.

[3] Emiliano Bellini. *Germanium-based solar cell tech for agrivoltaics*. 2021. URL: `https://www.pv-magazine.com/2021/01/15/germanium-based-solar-cell-tech-for-agrivoltaics/` (visited on 01/15/2023).

[4] Emiliano Bellini. *Longi claims world’s highest efficiency for silicon solar cells*. 2022. URL: `https://www.pv-magazine.com/2022/11/21/longi-claims-worlds-highest-silicon-solar-cell-efficiency/` (visited on 11/30/2022).

[5] Ayana Bhaduri et al. “Correlation of structural inhomogeneities with transport properties in amorphous silicon germanium alloy thin films”. In: *Solar Energy Materials and Solar Cells* 94.9 (2010). PVSEC 18, pp. 1492–1495. ISSN: 0927-0248. DOI: `https://doi.org/10.1016/j.solmat.2010.02.043`. URL: `https://www.sciencedirect.com/science/article/pii/S0927024810000966`.

[6] J. R. Blanco et al. “Density of amorphous germanium films by spectroscopic ellipsometry”. In: *Journal of Vacuum Science and Technology A* 4.3 (May 1986), pp. 577–582. ISSN: 0734-2101. DOI: `10.1116/1.573851`. eprint: `https://pubs.aip.org/avs/jva/article-pdf/4/3/577/11787741/577\_1\_online.pdf`. URL: `https://doi.org/10.1116/1.573851`.

[7] William H. Brune. *The Solar Spectrum*. 2023. URL: `https://www.e-education.psu.edu/meteo300/node/683` (visited on 03/29/2023).

[8] Fatma Ezzahra Cherif and Habib Sammouda. “Strategies for high performance perovskite/c-Si tandem solar cells: Effects of bandgap engineering, solar concentration and device temperature”. In: *Optical Materials* 106 (2020), p. 109935. ISSN: 0925-3467. DOI: `https://doi.org/10.1016/j.optmat.2020.109935`. URL: `https://www.sciencedirect.com/science/article/pii/S0925346720302810`.

[9] Jun-Ki Choi and Vasilis Fthenakis. “Crystalline silicon photovoltaic recycling planning: macro and micro perspectives”. In: *Journal of Cleaner Production* 66 (2014), pp. 443–449. ISSN: 0959-6526. DOI: `https://doi.org/10.1016/j.jclepro.2013.11.022`. URL: `https://www.sciencedirect.com/science/article/pii/S0959652613007865`.

[10] Valérie Depauw et al. “Wafer-scale Ge epitaxial foils grown at high growth rates and released from porous substrates for triple-junction solar cells”. In: *Progress in Photovoltaics: Research and Applications* (). DOI: `https://doi.org/10.1002/pip.3634`. eprint: `https://onlinelibrary.wiley.com/doi/pdf/10.1002/pip.3634`. URL: `https://onlinelibrary.wiley.com/doi/abs/10.1002/pip.3634`.

[11] T. D. Eales et al. “Ge1−xSnx alloys: Consequences of band mixing effects for the evolution of the band gap Γ-character with Sn concentration”. In: *Scientific Reports* 9.1 (2019), pp. 1–10. DOI: `10.1038/s41598-019-50349-z`. URL: `https://doi.org/10.1038/s41598-019-50349-z`.

[12] Editors of Encyclopaedia Britannica. *germanium*. `https://www.britannica.com/science/germanium`. Encyclopedia Britannica. June 2023.

[13] Larbi Filali. “Protein Adsorption on Hydrogenated Silicon Surfaces”. PhD thesis. Feb. 2018.

[14] Da Guo et al. “Metastability and reliability of CdTe solar cells”. English (US). In: *Journal Physics D: Applied Physics* 51.15 (Mar. 2018). ISSN: 0022-3727. DOI: `10.1088/1361-6463/aab1e1`.

[15] Wolfgang Guter et al. “Current-matched triple-junction solar cell reaching 41.1% conversion efficiency under concentrated sunlight”. In: *Applied Physics Letters* 94.22 (June 2009). 223504. ISSN: 0003-6951. DOI: `10.1063/1.3148341`. eprint: `https://pubs.aip.org/aip/apl/article-pdf/doi/10.1063/1.3148341/14415585/223504\_1\_online.pdf`. URL: `https://doi.org/10.1063/1.3148341`.

[16] Qiang Huang et al. “Single-Crystalline Germanium Thin Films by Electrodeposition and SolidPhase Epitaxy”. In: *Electrochemical and Solid State Letters - ELECTROCHEM SOLID STATE LETT* 10 (Jan. 2007). DOI: `10.1149/1.2771097`.

[17] Matt Hughes. *What is Plasma Enhanced Chemical Vapor Deposition (PECVD)?* 2022. URL: `https://www.semicore.com/news/118-what-is-plasma-enhanced-chemical-vapor-deposition-pecvd` (visited on 04/15/2023).

[18] IEA. *Solar PV*. 2022. URL: `https://www.iea.org/reports/solar-pv` (visited on 04/20/2023).

[19] Takashi Imajo, Takashi Suemasu, and Kaoru Toko. “Strain effects on polycrystalline germanium thin films”. In: *Scientific Reports* 11.1 (2021), p. 8333. DOI: `10.1038/s41598-021-87616-x`.

[20] Fraunhofer ISE. *Fraunhofer ISE Develops the World’s Most Efficient Solar Cell with 47.6 Percent Efficiency*. 2022. URL: `https://www.ise.fraunhofer.de/en/press-media/press-releases/2022/fraunhofer-ise-develops-the-worlds-most-efficient-solar-cell-with-47-comma-6-percent-efficiency.html` (visited on 05/30/2022).

[21] KAUST. *KAUST team sets world record for tandem solar cell efficiency*. 2023. URL: `https://www.kaust.edu.sa/en/news/kaust-team-sets-world-record-for-tandem-solar-cell-efficiency` (visited on 04/16/2023).

[22] Arjen Klaver. “Irradiation-induced degradation of amorphous silicon solar cells in space”. PhD thesis. May 2023.

[23] Taweewat Krajangsang et al. “Wide-Gap p- μ c- Si 1 - x O x :H Films and Their Application to Amorphous Silicon Solar Cells”. In: *International Journal of Photoenergy* 2013 (Jan. 2013). DOI: `10.1155/2013/958326`.

[24] J. Li et al. “A Brief Review of High Efficiency III-V Solar Cells for Space Application”. In: *Frontiers in Physics* 8 (2021). ISSN: 2296-424X. DOI: `10.3389/fphy.2020.631925`. URL: `https://www.frontiersin.org/articles/10.3389/fphy.2020.631925`.

[25] Jidong Long et al. “Doped Microcrystalline Silicon Layers for Solar Cells by 13.56MHz Plasma-enhanced Chemical Vapour Deposition”. In: *Energy Procedia* 15 (Dec. 2012), pp. 240–247. DOI: `10.1016/j.egypro.2012.02.028`.

[26] G. Lucovsky et al. “Chemical bonding of hydrogen and oxygen in glow-discharge–deposited thin films of a-Ge:H and a-Ge:(H,O)”. In: *Phys. Rev. B* 31 (4 Feb. 1985), pp. 2190–2197. DOI: `10.1103/PhysRevB.31.2190`. URL: `https://link.aps.org/doi/10.1103/PhysRevB.31.2190`.

[27] O. Madelung, U. Rössler, and M. Schulz, eds. *Germanium (Ge) Raman phonon frequencies and wavenumber*. 2001. DOI: `10.1007/10551045_228`. URL: `https://materials.springer.com/lb/docs/sm_lbs_978-3-540-31355-7_228`.

[28] Inès Massiot. “Design and fabrication of nanostructures for light-trapping in ultra-thin solar cells”. PhD thesis. Oct. 2013. DOI: `10.13140/RG.2.1.2731.0167`.

[29] I. M. Mathews. “Refractive index and density”. In: *Journal of the Franklin Institute* 177.6 (1914), pp. 673–686. DOI: `10.1016/S0016-0032(14)90992-9`.

[30] Sayantan Mazumdar, Ying Zhao, and Xiaodan Zhang. “Stability of Perovskite Solar Cells: Degradation Mechanisms and Remedies”. In: *Frontiers in Electronics* 2 (2021). ISSN: 2673-5857. DOI: `10.3389/felec.2021.712785`. URL: `https://www.frontiersin.org/articles/10.3389/felec.2021.712785`.

[31] Janne Meier et al. “High-Efficiency Amorphous and ”Micromorph” Silicon Solar Cells”. In: *Proceedings of the 3rd World Conference on Photovoltaic Energy Conversion* (June 2003), 2801–2805 Vol.3.

[32] ZG Meng et al. “ChemInform Abstract: Germanium Thin Film Formation by Low-Pressure Chemical Vapor Deposition”. In: *Cheminform* 28 (Aug. 2010). DOI: `10.1002/chin.199732012`.

[33] Dieter Mergel and Martin Jerman. “Density and refractive index of thin evaporated films”. In: *Chinese Optics Letters* 8 (Apr. 2010), pp. 67–72. DOI: `10.3788/COL201008S1.0067`.

[34] Vincenzo Muteri et al. “Review on Life Cycle Assessment of Solar Photovoltaic Panels”. In: *Energies* 13 (Jan. 2020), p. 252. DOI: `10.3390/en13010252`.

[35] Hisham Nasser. “Development Of Hybrid Photonic And Plasmonic Light Management Interfaces For Thin Film Semiconductor Devices”. PhD thesis. Aug. 2015.

[36] Justyna Pastuszak and Paweł Węgierek. “Photovoltaic Cell Generations and Current Research Directions for Their Development”. In: *Materials* 15.16 (Aug. 2022), p. 5542. ISSN: 1996-1944. DOI: `10.3390/ma15165542`. URL: `http://dx.doi.org/10.3390/ma15165542`.

[37] William Paul. “Structural, optical and photoelectronic properties of improved PECVD a-Ge:H”. In: *Journal of Non-Crystalline Solids* 137-138 (1991), pp. 803–808. ISSN: 0022-3093. DOI: `https://doi.org/10.1016/S0022-3093(05)80242-X`. URL: `https://www.sciencedirect.com/science/article/pii/S002230930580242X`.

[38] Li Qian et al. “High-quality Ge and Sn Thin Films Deposited on Si Substrate by Magnetron Sputtering”. In: *Procedia Engineering* 215 (2017). ICMAT 2017 Symposium (A to I), pp. 82–88. ISSN: 1877-7058. DOI: `https://doi.org/10.1016/j.proeng.2017.11.154`. URL: `https://www.sciencedirect.com/science/article/pii/S187770581733076X`.

[39] Z Remeš et al. “Optical determination of the mass density of amorphous and microcrystalline silicon layers with different hydrogen contents”. In: *Journal of Non-Crystalline Solids* 227-230 (1998), pp. 876–879. ISSN: 0022-3093. DOI: `https://doi.org/10.1016/S0022-3093(98)00207-5`. URL: `https://www.sciencedirect.com/science/article/pii/S0022309398002075`.

[40] P.J. Roelandschap, T. de Vrijer, and A.H.M. Smets. *Development of device quality a-Ge:H absorber layers by Plasma Enhanced Chemical Vapor Deposition*. 2021.

[41] H. Sai et al. “Triple-junction thin-film silicon solar cell fabricated on periodically textured substrate with a stabilized efficiency of 13.6%”. In: *Applied Physics Letters* 106 (21 2015), p. 213902. DOI: `10.1063/1.4921836`.

[42] B. Schröder et al. “Influence of oxygen incorporation on the properties of magnetron sputtered hydrogenated amorphous germanium films”. In: *Applied Physics Letters* 62.16 (Apr. 1993), pp. 1961–1963. ISSN: 0003-6951. DOI: `10.1063/1.109504`. eprint: `https://pubs.aip.org/aip/apl/article-pdf/62/16/1961/7791690/1961\_1\_online.pdf`. URL: `https://doi.org/10.1063/1.109504`.

[43] Patrick Schygulla et al. “Two-terminal III–V//Si triple-junction solar cell with power conversion efficiency of 35.9 % at AM1.5g”. In: *Progress in Photovoltaics: Research and Applications* 30.8 (), pp. 869–879. DOI: `https://doi.org/10.1002/pip.3503`. eprint: `https://onlinelibrary.wiley.com/doi/pdf/10.1002/pip.3503`. URL: `https://onlinelibrary.wiley.com/doi/abs/10.1002/pip.3503`.

[44] N. Sclar. “Properties of doped silicon and Germanium infrared detectors”. In: *Progress in Quantum Electronics* 9.3 (1984), pp. 149–257. ISSN: 0079-6727. DOI: `https://doi.org/10.1016/0079-6727(84)90001-6`. URL: `https://www.sciencedirect.com/science/article/pii/0079672784900016`.

[45] A. Shah et al. “Photovoltaic Technology: The Case for Thin-Film Solar Cells”. In: *Science* 285.5428 (1999), pp. 692–698. DOI: `10.1126/science.285.5428.692`. eprint: `https://www.science.org/doi/pdf/10.1126/science.285.5428.692`. URL: `https://www.science.org/doi/abs/10.1126/science.285.5428.692`.

[46] Y.H. Shing, J.W. Perry, and C.E. Allevato. “Amorphous silicon germanium alloy film deposition with in situ plasma diagnostics”. In: *Solar Cells* 24.3 (1988), pp. 353–362. ISSN: 0379-6787. DOI: `https://doi.org/10.1016/0379-6787(88)90087-7`. URL: `https://www.sciencedirect.com/science/article/pii/0379678788900877`.

[47] Santhosh Sivaraj et al. “A Comprehensive Review on Current Performance, Challenges and Progress in Thin-Film Solar Cells”. In: *Energies* 15.22 (Nov. 2022), p. 8688. ISSN: 1996-1073. DOI: `10.3390/en15228688`. URL: `http://dx.doi.org/10.3390/en15228688`.

[48] A. H. M. Smets, W. M. M. Kessels, and M. C. M. van de Sanden. “Surface-diffusion-controlled incorporation of nanosized voids during hydrogenated amorphous silicon film growth”. In: *Applied Physics Letters* 86.4 (Jan. 2005). 041909. ISSN: 0003-6951. DOI: `10.1063/1.1853508`. eprint: `https://pubs.aip.org/aip/apl/article-pdf/doi/10.1063/1.1853508/14327329/041909\_1\_online.pdf`. URL: `https://doi.org/10.1063/1.1853508`.

[49] V. Sorianello et al. “Micro-Raman characterization of Germanium thin films evaporated on various substrates”. In: *Microelectronic Engineering* 88.4 (2011). Post-Si-CMOS electronic devices: the role of Ge and III-V materials, pp. 492–495. ISSN: 0167-9317. DOI: `https://doi.org/10.1016/j.mee.2010.10.028`. URL: `https://www.sciencedirect.com/science/article/pii/S0167931710004004`.

[50] Vito Sorianello et al. “Low-temperature germanium thin films on silicon”. In: *Opt. Mater. Express* 1.5 (Sept. 2011), pp. 856–865. DOI: `10.1364/OME.1.000856`. URL: `https://opg.optica.org/ome/abstract.cfm?URI=ome-1-5-856`.

[51] Jaran Sritharathikhun et al. “Effect of the CO 2 /SiH 4 Ratio in the p- μ c-SiO:H Emitter Layer on the Performance of Crystalline Silicon Heterojunction Solar Cells”. In: *International Journal of Photoenergy* 2014 (June 2014), pp. 1–5. DOI: `10.1155/2014/872849`.

[52] M. Stuckelberger et al. “Comparison of amorphous silicon absorber materials: Light-induced degradation and solar cell efficiency”. In: *Journal of Applied Physics* 114.15 (Oct. 2013). 154509. ISSN: 0021-8979. DOI: `10.1063/1.4824813`. eprint: `https://pubs.aip.org/aip/jap/article-pdf/doi/10.1063/1.4824813/13897695/154509\_1\_online.pdf`. URL: `https://doi.org/10.1063/1.4824813`.

[53] Gianluca Timò et al. “Growth and Characterization of High Efficiency GaAlAs/GaAs/Ge Solar Cells”. In: *Materials Science Forum - MATER SCI FORUM* 203 (Feb. 1996), pp. 97–102. DOI: `10.4028/www.scientific.net/MSF.203.97`.

[54] S. Tobbeche, S. Kalache, M. Elbar, et al. “Improvement of the CIGS solar cell performance: structure based on a ZnS buffer layer”. In: *Optical and Quantum Electronics* 51 (8 2019), p. 284. DOI: `10.1007/s11082-019-2000-z`.

[55] Chao-Yang Tsao et al. “Low-temperature growth of polycrystalline Ge thin film on glass by in situ deposition and ex situ solid-phase crystallization for photovoltaic applications”. In: *Applied Surface Science* 255.15 (2009), pp. 7028–7035. ISSN: 0169-4332. DOI: `https://doi.org/10.1016/j.apsusc.2009.03.035`. URL: `https://www.sciencedirect.com/science/article/pii/S0169433209003018`.

[56] T. de Vrijer and Arno H. M. Smets. “Infrared analysis of catalytic CO2 reduction in hydrogenated germanium”. In: *Physical Chemistry Chemical Physics* 24.17 (2022), pp. 10241–10248. DOI: `10.1039/d2cp01054b`.

[57] Thierry de Vrijer et al. “The impact of processing conditions and post-deposition oxidation on the opto-electrical properties of hydrogenated amorphous and nano-crystalline Germanium films”. In: *Journal of Non-Crystalline Solids* 553 (2021), p. 120507. ISSN: 0022-3093. DOI: `https://doi.org/10.1016/j.jnoncrysol.2020.120507`. URL: `https://www.sciencedirect.com/science/article/pii/S0022309320306177`.

[58] Fuzhen Wang and Junwei Wu. “Chapter 10 - Plasma-enhanced chemical vapor deposition”. In: *Modern Ion Plating Technology*. Ed. by Fuzhen Wang and Junwei Wu. Elsevier, 2023, pp. 247–285. ISBN: 978-0-323-90833-7. DOI: `https://doi.org/10.1016/B978-0-323-90833-7.00010-3`. URL: `https://www.sciencedirect.com/science/article/pii/B9780323908337000103`.

[59] Marcin Wojdyr. “Fityk: a general-purpose peak fitting program”. In: *Journal of Applied Crystallography* 43.5-1 (2010), pp. 1126–1128. DOI: `https://doi.org/10.1107/S0021889810030499`. eprint: `https://onlinelibrary.wiley.com/doi/pdf/10.1107/S0021889810030499`. URL: `https://onlinelibrary.wiley.com/doi/abs/10.1107/S0021889810030499`.

[60] Yee-Chia Yeo et al. “Germanium-based transistors for future high performance and low power logic applications”. In: *2015 IEEE International Electron Devices Meeting (IEDM)*. 2015, pp. 2.4.1–2.4.4. DOI: `10.1109/IEDM.2015.7409613`.

A

Homogeneity of Samples

The thickness homogeneity of the samples was an important parameter to gauge the uniformity of depositions and can be used to predict the stability of the plasma. The thickness of the samples was normalized with respect to the centre. The values are listed for the initial 20 samples. Notes have been added for points with homogeneity of less than 90% to elicit the deposition condition that could have affected the plasma.

Table A.1: Homogeneity data

Sample	Sample point	Homogeneity	Average Homogeneity (%)	Notes
M18198	1	0.912	96.55	
	2	0.95		
	3	0.914		
	4	0.95		
	5	1		
	6	0.966		
	7	0.917		
	8	0.924		
	9	0.927		
M18199	1	0.92	91.9	
	2	0.92		
	3	0.87		
	4	0.94		
	5	1		
	6	0.94		
	7	0.88		
	8	0.93		
	9	0.87		
M18200	1	0.418	**71.98**	Power - 30 W
	2	0.425		
	3	0.407		
	4	0.704		
	5	1		
	6	0.656		
	7	0.974		
	8	0.985		

	9	0.91		
M18201	1	0.974	97.24	
	2	0.983		
	3	0.951		
	4	0.979		
	5	1		
	6	0.962		
	7	0.962		
	8	0.998		
	9	0.94		
M18202	1	0.918	97.27	
	2	0.96		
	3	0.958		
	4	0.995		
	5	1		
	6	0.995		
	7	0.979		
	8	0.993		
	9	0.955		
M18203	1	0.896	93.88	
	2	0.935		
	3	0.995		
	4	1.075		
	5	1		
	6	1.031		
	7	0.997		
	8	0.786		
	9	0.734		
M18204	1	0.847	**87.23**	Pressure - 8mbar
	2	0.85		
	3	0.841		
	4	0.855		
	5	1		
	6	0.9		
	7	0.862		
	8	0.856		
	9	0.84		
M18205	1	0.835	94.49	
	2	0.825		
	3	0.828		
	4	0.926		
	5	1		
	6	0.938		
	7	1.055		
	8	1.068		
	9	1.066		
M18206	1	1.046	101.13	
	2	0.991		
	3	0.973		

	4	1.034		
	5	1		
	6	1.043		
	7	1.014		
	8	0.994		
	9	1.006		
M18303	1	0.939	96.55	
	2	0.948		
	3	0.94		
	4	0.989		
	5	1		
	6	0.992		
	7	0.957		
	8	0.968		
	9	0.954		
M18304	1	0.942	96.52	
	2	0.966		
	3	0.938		
	4	0.968		
	5	1		
	6	0.968		
	7	0.961		
	8	0.99		
	9	0.953		
M18305	1	0.980	98.92	
	2	1.013		
	3	0.950		
	4	1.008		
	5	1		
	6	0.978		
	7	0.999		
	8	1.005		
	9	0.969		
M18306	1	0.85	92.70	
	2	0.947		
	3	0.909		
	4	0.942		
	5	1		
	6	0.964		
	7	0.885		
	8	0.938		
	9	0.908		
M18307	1	0.931	94.93	
	2	0.955		
	3	0.928		
	4	0.969		
	5	1		
	6	0.949		
	7	0.934		

	8	0.977		
	9	0.916		
M18308	1	0.913	94.61	
	2	0.940		
	3	0.909		
	4	0.976		
	5	1		
	6	0.95		
	7	0.934		
	8	0.977		
	9	0.916		
M18309	1	0.886	93.39	
	2	0.939		
	3	0.920		
	4	0.969		
	5	1		
	6	0.953		
	7	0.915		
	8	0.945		
	9	0.88		
M18310	1	0.735	**77.14**	Pressure - 6 mbar Germane content - 0.5%
	2	0.89		
	3	0.71		
	4	0.746		
	5	1		
	6	0.783		
	7	0.656		
	8	0.770		
	9	0.654		
M18311	1	0.869	96.77	
	2	0.908		
	3	0.874		
	4	0.975		
	5	1		
	6	0.975		
	7	1.034		
	8	1.057		
	9	1.017		
M18312	1	0.797	90.04	
	2	0.922		
	3	0.938		
	4	0.836		
	5	1		
	6	0.987		
	7	0.789		
	8	0.908		
	9	0.926		
M18313	1	0.83	86.85	
	2	0.874		

	3	0.805		
	4	0.895		
	5	1		
	6	0.878		
	7	0.854		
	8	0.866		
	9	0.815		

B

Optical Bandgap Analysis

The RT measurements of the sample were used to estimate the optical bandgap of the material. The following Matlab code first calculates the absorbance, and then plots it against photon energy. It calculates the intercept of the plot with the x-axis to give this value. If no intercept is found, the user can fit a manual line using the figure window to find a rough intercept.

```matlab
%This program roughly estimates the optical bandgap of the material from
%the absorbance profile.
%Inputs are the reflectance and transmission profiles

%Import data
filename = 'M18198';
ref_file = strcat('M:\ewi\ee\pvmd\pvmd-shared\Measurements\Hyet\Tasks\Tasks J - GeSn\Task J68 - reproduce GeH\First Deposition\Reflectance Data\',filename, '.Sample.raw.csv');
rf = readtable(ref_file);
tra_file = strcat('M:\ewi\ee\pvmd\pvmd-shared\Measurements\Hyet\Tasks\Tasks J - GeSn\Task J68 - reproduce GeH\First Deposition\Transmittance Data\',filename, '.Sample.raw.csv');
t = readtable(tra_file);
rf = renamevars(rf,["nm","x_R"],["Wavelength (nm)","R"]);
t = renamevars(t,["nm","x_T"],["Wavelength (nm)","T"]);

%Calculate absorbance and visualise
Absorbance = join(rf,t);
Absorbance.A = 100 - Absorbance.R - Absorbance.T;

plot(Absorbance.("Wavelength (nm)"),Absorbance.A);

%Plotting with photon energy and calculating intercept if exists, if not
%then manual line can be fit to find the intercept
h_nu = 1239.7./rf.("Wavelength (nm)");
Eopt = interp1(Absorbance.A,h_nu,0)

plot(h_nu, Absorbance.A);
xlim([0 4])
xticks(0:0.1:4)
ylim([-10 100])
xlabel("Photon energy (eV)")
ylabel("%A")
hold on
plot(Eopt, 0, 'm*', 'MarkerSize', 10);
yline(0)
hold off
```

C

Thickness Data

Data presented earlier in the report showed the deposition rate values. The following table gives the thickness values for all samples.

Table C.1: Thickness of all samples

Sample No.	Thickness (nm)	Deposition Conditions
M18198	1006	Pressure - 4,6,8 mbar Power - 10,20,30 W Germane Content - 1% Substrate Tempurature - 275 °C Deposition Time - 2000 s
M18199	1404	
M18200	1393	
M18201	1216	
M18202	1469	
M18203	1609	
M18204	1283	
M18205	1265	
M18206	1573	
M18303	229.3	Pressure - 4,5,6 mbar Power - 10 W Germane Content - ∼1%, ∼2%, ∼8%, 100% Substrate Temperature - 275 °C Deposition Time - 500 s
M18304	264	
M18305	652.3	
M18306	1012	
M18307	249	
M18308	287.4	
M18309	1716	
M18311	1071.2	
M18310	127	
M18312	193.4	
M18313	564	
M18314	1408	
M18503	86.2	Pressure - 4 mbar, Power - 10 W Germane Content - 0.5%, 1%, 1.5% Substrate Temperature - 225 °C 275 °C, 275 °C (with early ignition) Deposition Time - 500 s
M18504	76.6	
M18505	156	
M18506	78.7	
M18507	41.8	
M18508	184.4	
M18509	97.6	

M18510	29.9	
M18511	336.5	

D

EdX Data

EdX measurements were performed to detect the signature of oxygen after 2 months of air exposure. 5 samples were measured for signature. One of them was shown in chapter 4. The results for the rest of the samples are covered here.

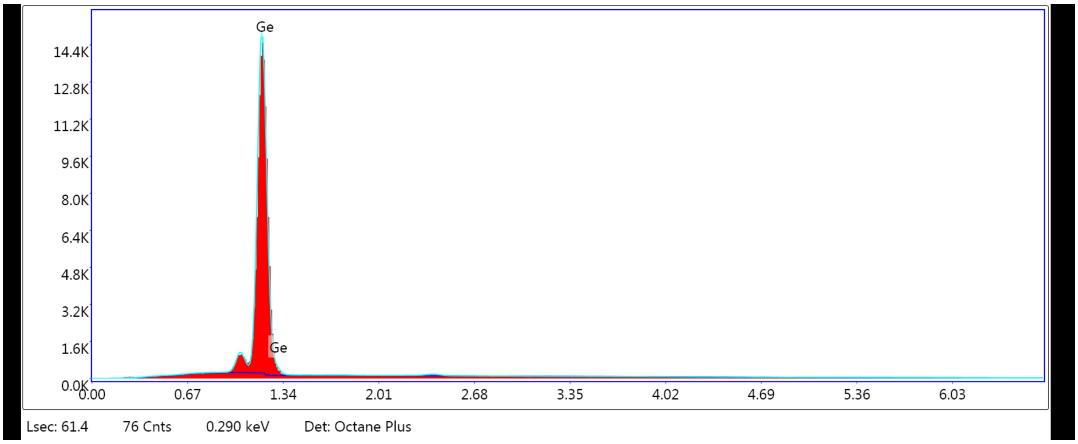

(a) M18199 measured before exposure

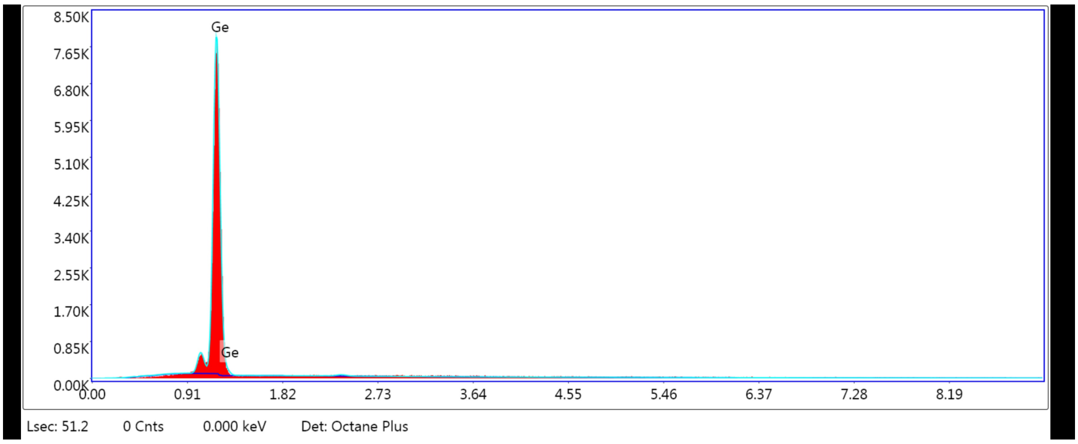

(b) M18199 measured after two months

Figure D.1: Results of EDX testing for M18199 measured initially and after two months exposure

M18199 (Figure D.1) was taken from the first series, where the samples were over a micron thick due to a high deposition time of 2000 s. No oxygen signature was detected.

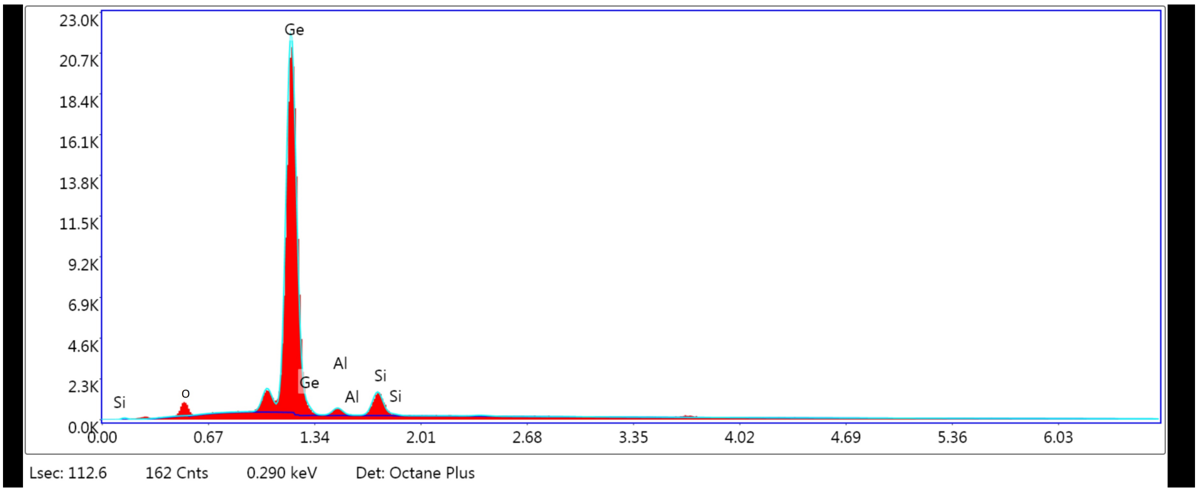

(a) M18303 measured before exposure

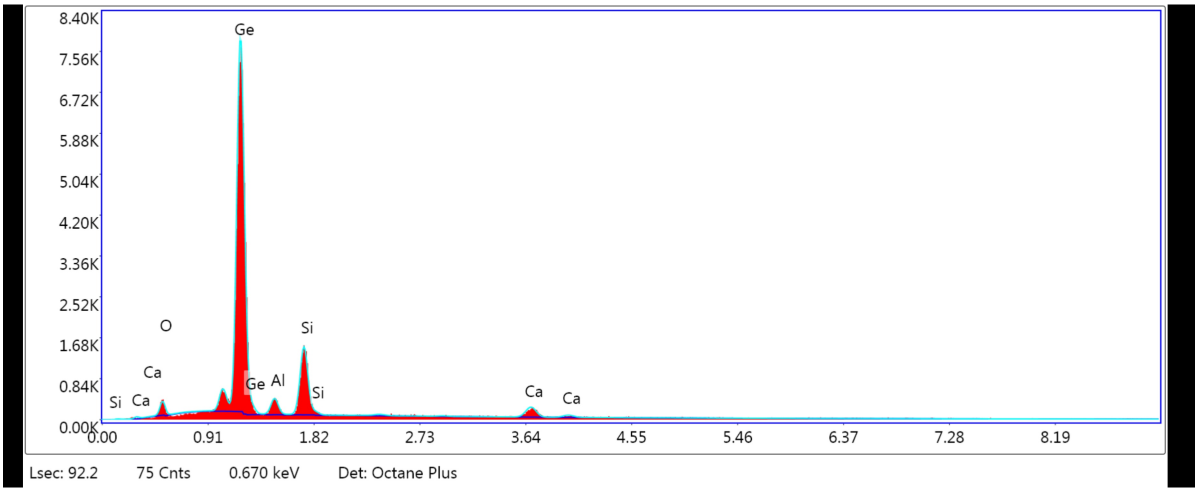

(b) M18303 measured after two months

Figure D.2: Results of EDX testing for M18303 measured initially and after two months exposure

M18303 (Figure D.2) was picked from the second series of depositions where the deposition time was 500s. This led to a thinner film deposition and thus, there is a silicon and oxygen signature observed from the substrate. The relative peak of Ge to Oxygen is still found to not change after 2 months. Although Si signature is observed to rise, it is possible that Silicon may have diffused into the sample over this time period. The presence of Al and Ca can be attributed to contamination from surroundings or impurities in the substrate.

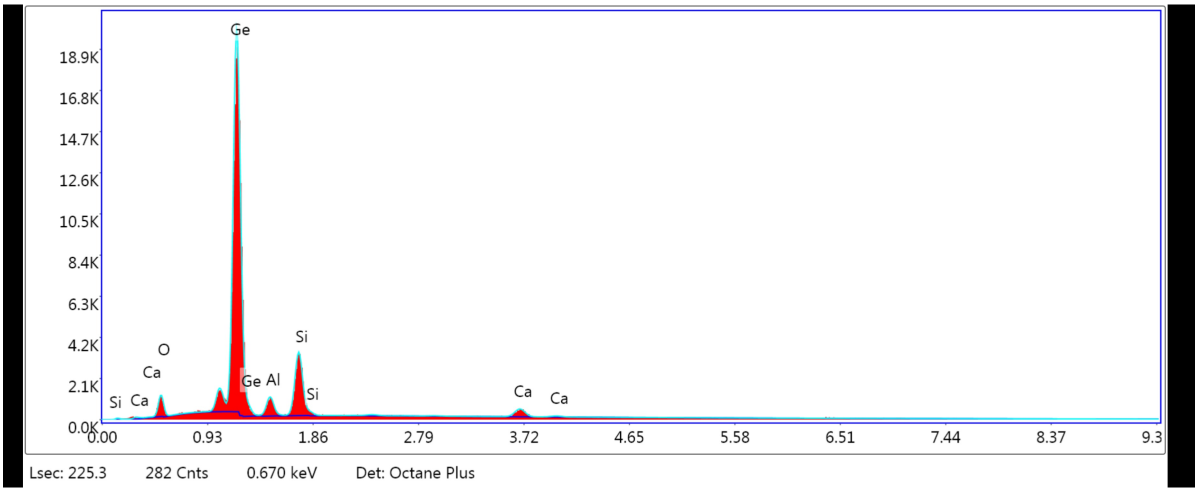

(a) M18304 measured before exposure

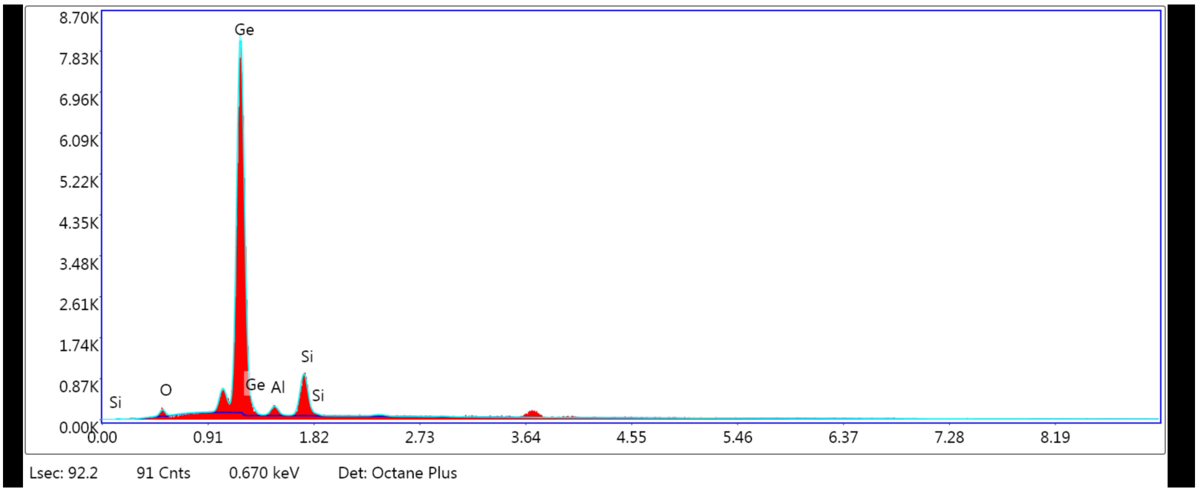

(b) M18304 measured after two months

Figure D.3: Results of EDX testing for M18304 measured initially and after two months exposure

A similar pattern is seen for M18304 (Figure D.3), another one of the thinner samples with no extra oxygen signature.

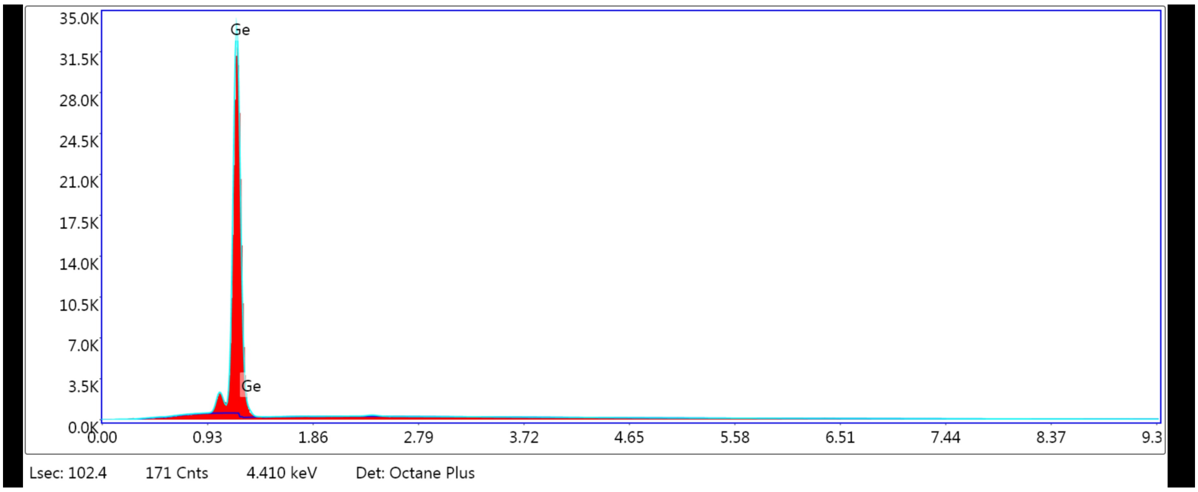

(a) M18306 measured before exposure

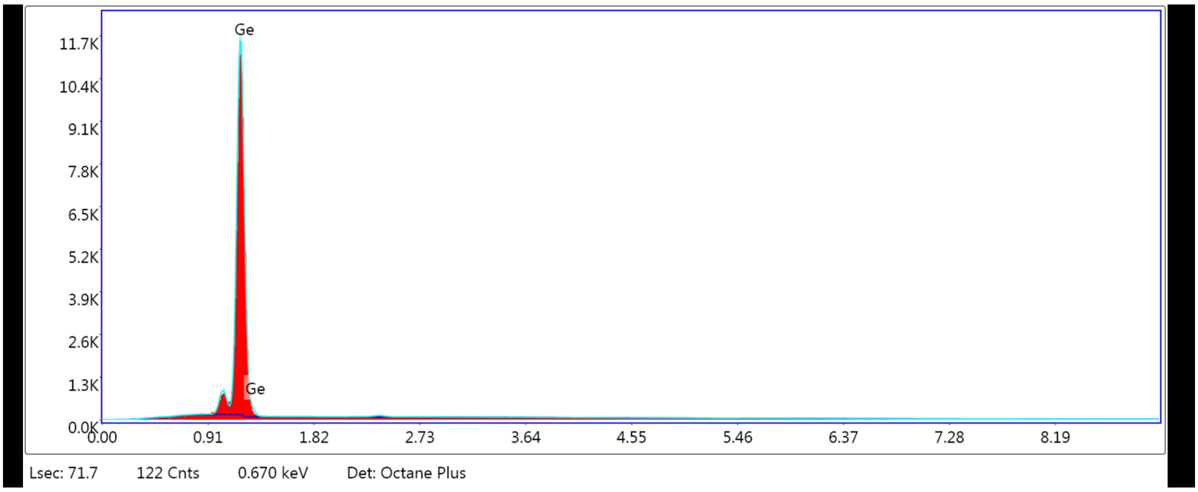

(b) M18306 measured after two months

Figure D.4: Results of EDX testing for M18306 measured initially and after two months exposure

M18306 (Figure D.4) was also picked from the second series. This sample was deposited with germane flow only and was found to be over a micron thick. Thus, no Si or oxygen signature was seen from the substrate.

E

Intrinsicity

Data related to the bandgap, activation energy and intrinsicity are the most important parameters when characterizing a low-bandgap material. This data is presented here. Samples are divided as per their deposition condition series. Intrinsicity is calculated as follows

$$Intrinsicity = \frac{E_{act}}{E_{04}} \tag{E.1}$$

Table E.1: Bandgap, activation energy and intrinsicity data for all samples

Sample No.	E_{04} (eV)	E_{opt} (eV)	E_{act}	Intrinsicity
M18198	0.84	0.805	0.454	0.54
M18199	0.83	0.895	0.428	0.516
M18200	0.8	0.778	0.39	0.487
M18201	0.86	0.84	0.454	0.54
M18202	0.81	0.81	0.311	0.385
M18203	0.73	0.72	0.137	0.188
M18204	0.89	0.86	0.425	0.477
M18205	0.84	0.86	0.228	0.272
M18206	0.74	0.69	0.224	0.303
M18303	0.895	0.938	0.259	0.29
M18304	0.88	0.94	0.262	0.297
M18305	0.924	0.922	0.413	0.447
M18306	0.92	0.819	0.402	0.437
M18307	0.88	0.906	0.336	0.382
M18308	0.93	0.918	0.384	0.413
M18309	0.88	0.885	0.33	0.375
M18312	0.93	0.784	0.249	0.268
M18310	0.95	0.829	0.241	0.254
M18311	1	1.026	0.296	0.296
M18313	0.875	0.903	0.276	0.315
M18314	0.89	0.8	0.341	0.383
M18503	1.014	0.91	0.36	0.355
M18504	1.03	1.01	0.375	0.364

M18505	0.994	1.05	0.412	0.414
M18506	1.027	0.99	0.34	0.331
M18507	0.993	0.97	0.208	0.209
M18508	0.97	0.96	0.347	0.358
M18509	0.847	0.88	0.38	0.448
M18510	0.986	0.95	0.215	0.218
M18511	0.85	0.88	0.462	0.543